Direct Absorption and Photoacoustic Spectroscopy for Gas Sensing and Analysis: A Critical Review

Alaa Fathy, Yasser M Sabry, Ian W Hunter, Diaa Khalil, Tarik Bourouina

LASER & PHOTONICS REVIEWS
www.lpr-journal.org

Direct Absorption and Photoacoustic Spectroscopy for Gas Sensing and Analysis: A Critical Review

*Alaa Fathy, Yasser M. Sabry, Ian W. Hunter, Diaa Khalil, and Tarik Bourouina**

Optical spectroscopy has a broad scientific basis in chemistry, physics, and material science, with diverse applications in medicine, pharmaceuticals, agriculture, and environmental monitoring. Fourier transform infrared (FTIR) spectrometers and tunable laser spectrometers (TLS) are key devices for measuring optical spectra. Superior performance in terms of sensitivity, selectivity, accuracy, and resolution is required for applications in gas sensing. This review deals with gas measurement based on either direct optical absorption spectroscopy or photoacoustic spectroscopy. Both approaches are applicable to FTIR spectroscopy or TLS. In photoacoustic spectroscopy, cantilever-based photoacoustic spectroscopy is focused due its high performance. A literature survey is conducted revealing the recent technological advances. Theoretical fundamental detection limits are derived for TLS and FTIR, considering both direct absorption and photoacoustic spectroscopies. A theoretical comparison reveals which technology performs better. The minimum normalized absorption coefficient and normalized noise equivalent absorption coefficient appear as key parameters for this comparison. For TLS-based systems, direct absorption spectroscopy is found to be the best for lower laser power and longer path length. For FTIR-based systems, direct absorption is found to be the best for low temperature sources, higher spectrometer throughput, faster mirror velocity, and longer gas cells.

1. Introduction

Spectroscopy is widely used for the analysis of a broad range of materials in solid, liquid, gas, and plasma states. Gas-sensing based on spectroscopy is used extensively in the chemical industry, material sciences, oil refineries, and the pharmaceutical industry. It is also increasingly adopted for applications in the food industry, precision agriculture, and environmental monitoring. It is crucial for measurements of air pollution such as indoor air quality control, monitoring pollution outdoors, and the study of greenhouse gases emissions and their dispersion. Gas measurement can be conducted using electrochemical sensors, metal oxide semiconductors, gas chromatographs, mass spectrometers or optical spectrometers.[1] Optical methods are more compatible with real-time/continuous measurements as compared to gas chromatography for example.[2] The different forms of optical spectroscopy include atomic emission spectroscopy, Raman spectroscopy, and fluorescence spectroscopy, but these are not considered in this review.

Absorption spectroscopy is the most widespread technique used for gas analysis and probably the most suitable. The main techniques used in absorption spectroscopy include nondispersive infrared spectroscopy, tunable laser spectroscopy (TLS) and Fourier transform infrared (FTIR) spectroscopy. Among the different detection methods, TLS is characterized by its high sensitivity and excellent spectral resolution, whereas FTIR is characterized by its wide infrared spectral range covering the absorption molecular spectrum of a broad variety of gases.

Measurement of the amount of light absorbed by a gas can be conducted using either an optical detector or a photoacoustic cell. In the former case, we refer to direct absorption spectroscopy (DAS) whereas in the latter case, the term photoacoustic spectroscopy (PAS) is used. Increasing the optical path length is required to enhance the detection limits of gas concentrations. This can be implemented in a limited foot-print space using multipass (MP) gas cells or using a resonant optical cavity. Such enhancement is crucial in several applications that require high sensitivity such as the detection of volatile organic compounds (VOCs) in indoor environments where detection limits of parts per billion (ppb) concentration levels are often required for

A. Fathy, T. Bourouina
Université Gustave Eiffel
ESYCOM CNRS UMR 9007
Noisy-le-Grand ESIEE Paris – 93162, France
E-mail: tarik.bourouina@esiee.fr
A. Fathy, D. Khalil
Si-Ware Systems
3 Khalid Ibn Al-Waleed St., Heliopolis, Cairo 11361, Egypt
A. Fathy, Y. M. Sabry, D. Khalil
Ain-Shams University
Faculty of Engineering
1 Elsarayat St. Abbasseya, Cairo 11535, Egypt
I. W. Hunter
BioInstrumentation Lab
Department of Mechanical Engineering
Massachusetts Institute of Technology
Cambridge, MA 02139, USA

DOI: 10.1002/lpor.202100556

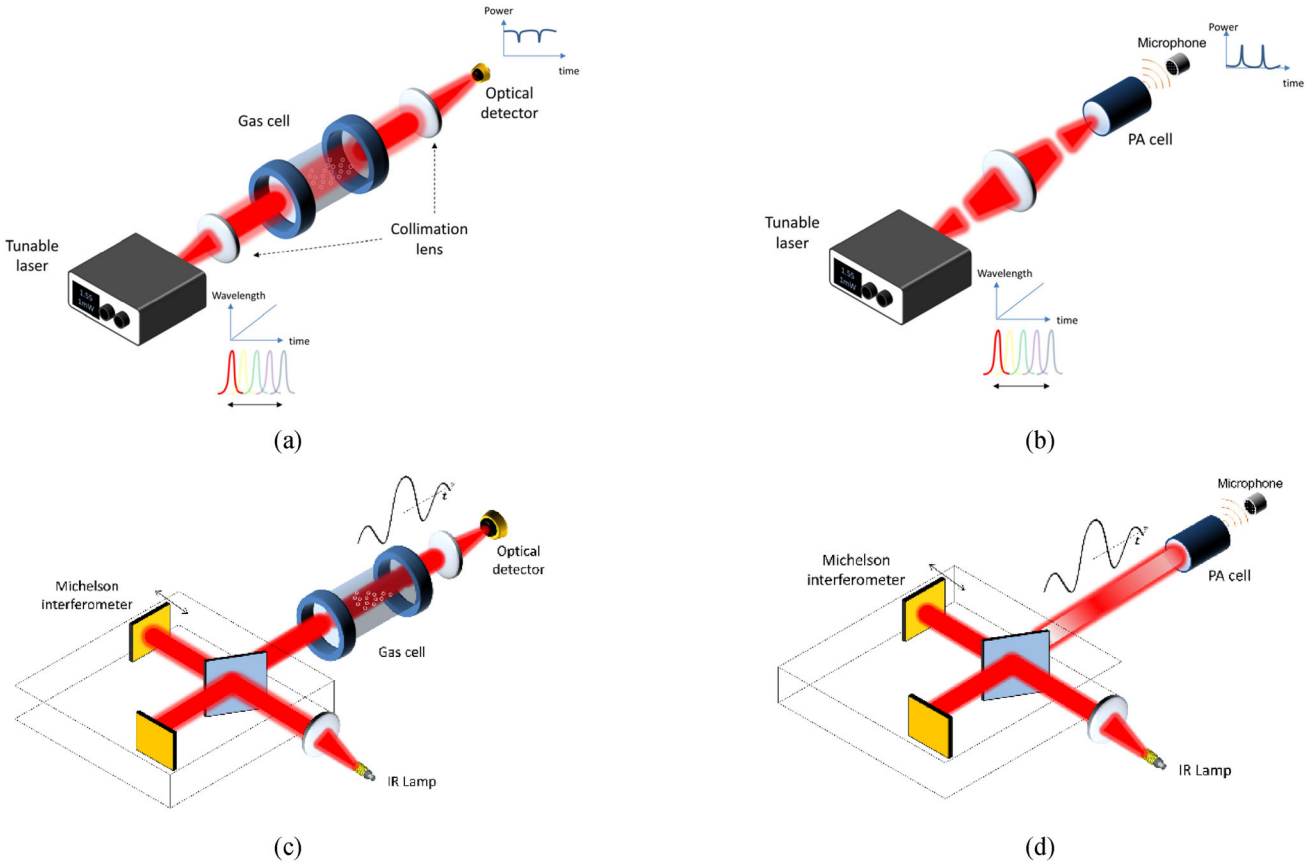

Figure 1. Different gas sensing techniques. a) 3D view of direct absorption spectroscopy using a tunable laser diode. b) 3D view of PAS systems using a modulated tunable laser diode. c) DAS based on an FTIR spectrometer comprising a Michelson interferometer, a gas cell and an optical detector. d) PAS based on a FTIR spectrometer comprising a Michelson interferometer, a PA cell, a microphone (cantilever), and another interferometer (not shown) for the PA signal detection.

addressing possible health consequences associated with those VOCs. Such high sensitivity levels are also required in some outdoor environments, such as monitoring the dispersion of atmospheric pollutants, including greenhouse gases that contribute to global warming[3] or for early stage detection and localization of gas leakages around hazardous gas plants.

Within the DAS category, TLS is used to identify systems that use a tunable laser followed by a gas cell and then an optical detector, as depicted in **Figure 1**a. The transmitted light after gas absorption is the detected signal. Laser spectroscopy is distinguished by its high power and excellent spectral resolution, which enables excellent gas selectivity; however, it has a limited tunability, in the order of 50–200 nm, resulting in restricting the spectral range as compared to FTIR spectrometers, whose spectral range is in the order of 2000–20 000 nm. This high sensitivity of TLS has led to detection limits in the order of parts per trillion (ppt) using MP cells. For example, a detection limit of ammonia (NH_3) of 200 ppt was achieved for a 1 s measurement time and a path length of 76 m, whereas for the same configuration it was 300 ppt for nitric oxide (NO).[4] A detection limit of 20 ppb of methane (CH_4) was reported[5] using a Herriot cell of path length of 252 m and measurement time of 2 s.

FTIR spectrometers use a broadband source in contrast to the lasers' narrowband widths, in conjunction with an interferometer, which is typically a Michelson configuration, as depicted in Figure 1c. FTIR spectrometers can simultaneously analyze multispecies within a wide range of infrared absorption spectra.[6] They also have a high spectral resolution, but it is lower than that of the TLS in addition to its lower spectral power density. FTIR spectrometers have better tolerance against different gases interferences by applying multivariate analysis,[7] a kind of machine-learning approach. It has been used for many years for the detection of air pollutants. The detection limits of FTIR spectrometers can be enhanced using long path cells (up to hundreds of meters), which enables concentrations as low as the ppb range or even lower to be measured.[8,9] Recently, miniaturized MEMS spectrometers have proven to be a compact solution for air monitoring with a low sensitivity (sub ppm range detection limits).[10] In general, FTIR-based DAS is applicable for studying gas reactions,[11,12] gas emissions,[13–15] measuring atmospheric trace gases and greenhouse gases flux,[16] open path measurements,[3,17–21] and airborne measurements.[22]

The PAS category has two configurations, similar to the TLS or FTIR in the DAS category. The first configuration is similar to TLS except that a modulator, and a microphone is used instead of the optical detector. This is depicted in Figure 1b. The output light from the laser, is modulated using either an electrical or a mechanical modulator. The modulated light is then absorbed

by the gas. The gas absorption of such modulated light leads to the emission of an acoustic pressure wave which is detected by the microphone. The gas is contained in an acoustic cell which can be operated at resonance or not. The cell configurations include 1D cylindrical resonators, Helmholtz resonators or cavity resonators.[23]

In the FTIR configuration, the modulated output from an interferometer, which is illuminated by a broadband source, passes through the gas. This modulated optical intensity is converted into an acoustic wave, which is then detected by a microphone. This system is depicted in Figure 1d.

The photoacoustic-based system is characterized by its independence on the gas cell length, which permits the use of small volume gas cells instead of the large ones used in the DAS scheme. However, this can be seen as a disadvantage, since the detection limit cannot be enhanced by increasing the path length. Thus, DAS has a superior performance when large gas cells are used. Another advantage is that the measured signal is directly related to the absorbed power not the transmitted one as in TLS. The pioneering microphone type for TLS and FTIR is the one based on the cantilever, which has much higher sensitivity than conventional electret microphones. PAS has a tremendous range of applications such as trace-gases monitoring,[23] open-air measurements,[24] smoke detectors,[25] breath analysis,[26] automotive emissions,[27] radioactive components analysis,[28] manned spaceships,[29] biological and medical applications, microbiology,[30] and even in the analysis of the status of power transformers.[31] Regarding its sensitivity, with lasers PAS shows good performance for small gas lengths (<100 mm).[32] As an example,[33] using a photoacoustic (PA) cell of 95 mm long and a laser power of 0.95 W, a detection limit of 0.65 ppt of hydrogen fluoride (HF) was obtained within a measurement time of half an hour.

It is apparent that the PAS shows good performance for short cells (20 mm or less) while direct absorption spectroscopy TLS (Direct TLS) has better sensitivity for longer cells.[32] However, some questions remain, namely, which detection scheme is more sensitive given a certain laser power and particular gas cell length. To answer this question, a comparison is needed between the two detection systems in the case of TLS for a given power and in the case of FTIR for a given spectral resolution, throughput, and interferometer mirror velocity. This comparison was conducted by deriving the theoretical fundamental detection limits of the different detection schemes. The related theoretical equations show the limiting parameters of each system alone compared with its respective technology. The figure of merit for this comparison is the normalized absorption coefficient defined as the minimum detectable absorption coefficient normalized for the measurement bandwidth ($cm^{-1}Hz^{-0.5}$). In addition, the normalized noise equivalent absorption (NNEA) coefficient (cm^{-1} W $Hz^{-0.5}$), commonly used in PAS, is also employed for these comparisons for laser spectroscopy. A review of the literature was also conducted for TLS and FTIR approaches using cantilever-based PAS or DAS. This was not only intended to show the latest advancements in these fields, but also to summarize the real achieved detection limits and make further comparisons resulting from an analysis based on the proposed theoretical framework. This paper is organized as follows: Section 2 reviews the published work using TLS in both the DAS and cantilever-based PAS modes. The theoretical fundamental detection limits of both systems are derived and compared. Section 3 reviews research using FTIR in both the DAS and cantilever-based PAS modes. The corresponding theoretical fundamental detection limits are also derived. Finally, in the conclusions we summarize the main results of this critical review.

2. Tunable Diode Laser System

2.1. Laser-Based DAS

The TLS system is depicted in Figure 1a, where the output power from the tunable laser source, at a given wavelength λ and power P_o, is coupled into a gas cell using collimation optics (e.g., a lens). The collimated light traveling in the gas cell interacts with its gaseous content. At the output from the gas cell, light is refocused onto the detector for conversion into an electrical signal. The laser's wavelength is tuned at a given gas absorption line. To detect another absorption line or another gas, the laser must be tuned to the respective wavelength. The linewidth of lasers can be as low as a few MHz or even less.[34–38] On the other hand, the linewidth of gases is a few GHz at atmospheric pressure,[32,35,39–41] while at reduced pressure linewidths can reach tenths of MHz.[42,43] Thus, the laser linewidth is much smaller than the gas linewidth.

2.1.1. Theoretical Fundamental Detection Limit of Laser-Based DAS

Shot noise, thermal noise, quantization noise, and flicker noise represent the different noise types in the optical detector-based systems. The shot noise represents the theoretical fundamental noise limit for such systems, and it is given by

$$i_n = \sqrt{2qi\Delta f} \tag{1}$$

where i is the total detector current, q is the elementary charge of an electron, and Δf is the noise bandwidth (single sided).

In order to compare different detectors of different areas, a figure of merit called the specific detectivity is used and is expressed as

$$D^* = \frac{\sqrt{A_d}}{NEP} \tag{2}$$

where A_d is the detector area and NEP (W $Hz^{0.5}$) represents the equivalent optical power of noise when the signal to noise ratio SNR is equal to 1 and is given by[44]

$$NEP = \frac{i_n}{R_i\sqrt{\Delta f}} \tag{3}$$

where i_n is the current noise and R_i is the detector current responsivity (A W^{-1}).

The equivalent power of the detector signal at a given wavelength, λ, is given by ($\alpha l \ll 1$)

$$P_{detector}(\lambda) = P_o(\lambda)\,\zeta\,(1-\alpha(\lambda)\,l) + NEP\sqrt{\Delta f} \tag{4}$$

where l is the gas interaction length, $\alpha(\lambda)$ is the wavelength dependent absorption, $P_o\zeta\alpha l$ represents the amount of power absorbed by the gas, $P_o(\lambda)$ is the laser power at given wavelength, and ζ is the coupling coefficient from the laser output to the detector. Thus, one can define SNR as

$$\mathrm{SNR}(\lambda) = \frac{P_o \alpha(\lambda) l\zeta}{\mathrm{NEP}\sqrt{\Delta f}} \tag{5}$$

Then, the minimum normalized absorption coefficient (normalization means to be normalized to square root of measurement bandwidth) is given by

$$\alpha_{\min \mathrm{DAS}}(\lambda) = \frac{\alpha(\lambda)}{\mathrm{SNR}(\lambda)\sqrt{\Delta f}} = \frac{\mathrm{NEP}}{P_o(\lambda) l\zeta} \tag{6}$$

The total detector current, is the sum of the currents due to the laser power and background power. It is given by

$$i = P_o\ \zeta\ R_i(\lambda) + \int_0^{\lambda} B_{\mathrm{BG}}(\lambda')\,\mathrm{TP_d} R_i(\lambda')\,\mathrm{d}\lambda' \tag{7}$$

where $\mathrm{TP_d}$ is the detector throughput in Sr m^2 and B_{BG} represents the spectral radiance (per unit wavelength) of the black body source at temperature T_{BG} in W $\mathrm{Sr}^{-1}\mathrm{m}^{-2}$ m^{-1}. The first term represents the contribution from the output power from the laser (percentage absorbed by the gas is neglected), while the second term represents the contribution of the background power. The maximum limit of the integration in Equation (7) is the peak sensitivity of the detector and also the cutoff wavelength in semiconductor detectors.[45] The first term dominates the second term for the range of laser power used in gas sensing (few mW up to W). Also, the laser spot size is within a few micrometers, meaning that the detector area can be reduced significantly leading to small thermal and background noise. Thus, the second term can be neglected. In view of Equations (1), (3), (6), and (7) the corresponding $\alpha_{\min}$ is obtained as follows

$$\alpha_{\min \mathrm{DAS}} = \frac{1}{l}\sqrt{\frac{2q\zeta}{R_i(\lambda) P_o}} \tag{8}$$

As can be seen, the minimum absorption coefficient is inversely proportional to $\sqrt{P_o}$. The responsivity equation is given by $\frac{\eta q \lambda}{hc}$ $(\lambda : 0 \rightarrow \lambda_c)$, where η is the detector quantum efficiency, q is the electron charge, h is Plank's constant, and λ_c is the cut-off wavelength of the detector. Increasing the wavelength results in a better detection limit, due to the increased number of photons (better responsivity). A comparison of the results from research on TLS can be found in **Table 1**. The corresponding $\alpha_{\min}$ was calculated using Equation (8). Practically, the maximum power, due to detector saturation, limits $\alpha_{\min}$. The detector saturation limit can be increased by raising the detector reverse bias voltage (limited by detector characteristics), decreasing the load resistance and using power meter (amplifiers) of wider input current range.

2.1.2. Survey on Laser-Based DAS Systems

Lasers: In TLS, the laser source can be a diode laser, interband cascade laser (ICL) or a quantum cascade laser (QCL). The physical mechanism of the laser diode is characterized by the conversion efficiency of photons into electrons at fixed and stable wavelengths. Increasing the emission wavelength of a diode laser requires a smaller bandgap that is closer to the background thermal fluctuations.[32] In addition, more nonradiative losses are encountered due to increased Auger recombination.[84,85] An example of such a laser operating in the mid-infrared MIR spectral range is the lead salt laser. It can operate over a large spectral range in the IR region (3.3 to 29 μm)[84,86] but operates under cryogenic conditions and has low power emission of few mW.[87] Therefore, QCL and ICL are used for the MIR spectral range.

The QCL was first demonstrated in 1994.[88] The QCL is based on a periodic structure of multiple quantum wells. Each quantum well introduces discrete electronic states within the band, where photon emission occurs in-between (intersubband/intraband transition). The spacing between the states and, thus, the emission wavelength is determined by the thickness of the layers. After that, the electron tunnels to the next quantum well (intraband tunneling), emits a photon and so on. The multiple photons emitted by a single electron raises the efficiency of such a laser. Over the last decade, there have been successful efforts in increasing the overall efficiency of QCL for both continuous and pulsed operation.[36] The QCL appears as a strong candidate for mid-infrared gas sensing from 4 to 15 μm and even in the terahertz range.[32] The idea of stacking different wavelength quantum cascade stages was exploited for covering a large spectral range from 5.9 to 10.9 μm using the same device with a peak power around 50 mW.[89] The main disadvantage of QCLs is the large threshold current, and thus the high power consumption.[85,90] Also, the QCL performance is still limited for wavelengths less than 4 μm.[34,85] The ICL, like the QCL, is based on cascading multiple layers, and like laser diodes where transitions occur between the conduction and the valence band (interband transitions). After photon emission, the electrons tunnel to the next layer through interband tunneling from the valence band to the conduction band of another layer and so on. The ICL is the choice for applications requiring low power consumption.

In its simplest form, the feedback in the laser system is implemented using two mirrors forming a Fabry–Pérot cavity, which is characterized by its rather large bandwidth leading to multimode lasing. This can be mitigated with a narrowband feedback operation using a diffraction grating on the top of active layer, described as a distributed feedback DFB laser. This method can be applied to laser diodes, QCL and ICL. Another approach is to apply a multilayer Bragg reflector on the top and bottom of the active layer, where the laser beam is emitted vertically. Thus, it is called a vertical cavity surface emitting laser. It can also be applied to laser diodes, QCL[91] and ICL.[92] For a wider tuning range, an external cavity is used to tune the wavelength using the laser active medium and, for example, a grating as the wavelength selection component.

Difference frequency generation is a concept used to generate a tunable mid-infrared laser for gas sensing applications.[93] It is based on focusing two seed lasers of different wavelengths (called signal and pump laser, respectively) into a nonlinear optical medium. Due to the nonlinearity, an idler beam of difference frequency of the input lasers is generated. Making use of the well-engineered tunable near IR laser sources as one of the

Table 1. Comparison of different gas measurements made using TLS. The table is sorted according to each gas species. In the table comparison is made with respect to the optical source, gas cell, detector type, and the minimum detectable concentration (CW stands for continuous; WM stands for wavelength modulation; MP stands for multipass cell; D stands for diameter; and BP stands for the base-path length of multipass cell).

				Gas cell								
Laser type	Power [mW]	Laser modulation	Wavelength [μm]	Type	Length [m]	Detector type	Pressure [Torr]	Gas	Integration time [s]	Detection limit/	α_{min}[cm^{-1}]×10^{12}	Ref.
DFB	–	WM-2f	1.533	Herriot with dual paths	20/6	InAsSb	760	Acetylene (C_2H_2)	2	4/7.9 ppm	–	[46]
DFB	–	FMS	1.51	Herriott	17.5	InGaAs	70	C_2H_2	166	18 ppb	–	[47]
ICL	2.5–3	WM-2f/1f	3.345	Herriott	10.5	MCT	750	Ethanol (C_2H_5OH)	<0.6	28 ppb	0.2	[48]
Tunable QCL	20	–	5.5–10	Herriott	76	MCT	675–750	C_2H_5OH	–	10–50 ppb	–	[49]
Tunable QCL	20	–	5.5–10	Herriott	76	MCT	675–750	C_3H_6O	–	10–50 ppb	–	[49]
CW DFB	1.75	WM-2f	3.359	MP. (BP 12.5 cm)	57.6	TEC-MCT	200	Methyl vinyl (C_2H_6)	1	740 ppt	0.05	[50]
CW-TEC-DFB- ICL	9	WM-2f/1f	3.337	Dense MP.	54.6	TEC-MCT	<100	C_2H_6	208	299/239 ppt	0.02	[51]
CW-ICL	–	DAS	3.3368	MP	54.6	TEC-PV-MCT	100	C_2H_6	166	777 ppt	–	[52]
CW-ICL	–	WM	3.3368	MP	54.6	TEC-PV-MCT	100	C_2H_6	108	269 ppt	–	[52]
–	4.5	WM-2f	1.318	–	0.8	InGaAs	–	Methane (CH_4)	–	20 ppm	3.2	[53]
QCL	–	WM-2f	7.8	MP (BP = 16.9 cm)	57.6	–	200	CH_4	1	5.9 ppb	–	[54]
ICL	–	WM-2f	3.291	MP	16	MCT PC	750	CH_4	2	5.8/13.1ppb	–	[55]
External cavity- QCL	<87	WM-2f	7.968	MP	152	MCT	50	CH_4	1	4.8 ppb	0.002	[56]
DFB	5.34	WM	1.654	–	0.4	InGaAs	–	CH_4	1	29.52 ppm	5.3	[57]
DFB-QCL	120	WM-2f	7.7072	Herriott	76	TEC-PV-MCT	80	CH_4	2	8.5 ppb	0.003	[58]
DFB-ICL	–	DAS	3.3	Integrating sphere (D:10 cm)	0.545	Cooled MCT	750	CH_4	–	1 ppm	–	[59]
QCL	–	WM	7.82	Hollow silica WG (D:1 mm)	5	TEC-MCT	750	CH_4	2	260 ppb	–	[60]
DFB laser	–	WM-2f	1.654	Direct gas cell	1.45	–	–	CH_4	–	100 ppb	–	[61]
ICL	–	WM -2f/1f	3.392	HWG (D:1 mm)	0.75	TEC-InAsSb	760	CH_4	9	6.7 ppb	–	[62]
DFB	–	WM with wavelet denoising	1.65	Direct gas cell	0.2	InGaAs	–	CH_4	500	80 ppb	–	[63]
CLaDS	–	Chirped laser	1.65	Open path	100	InGaAs	–	CH_4	10	<10 ppb	–	[64]
DFB	–	WM-2f	1.65	MP	–	–	–	CH_4	900	0.44 ppb	–	[65]
DFB	10	WM-2f	1.653	Open path	1300	InGaAs	760	CH_4	1	2 ppb	–	[66]
ICL	10	WM-2f	3.37	MP	580	TEC-MCT	760	CH_4	290	0.56 ppb	–	[67]
Lead salt diode	–	–	4.618 & 4.709	Astigmatic Herriott	36	MCT	0.05–0.06	Carbon monoxide (CO)	3	3 ppb	–	[68]
–	–	WM-2f	2.33	Herriott	14.5	–	0.93	CO	0.6	40 ppb	–	[69]

(*Continued*)

Table 1. (Continued).

Laser type	Power [mW]	Laser modulation	Wavelength [μm]	Gas cell		Detector type	Pressure [Torr]	Gas	Integration time [s]	Detection limit/	α_{min}[cm^{-1}]×10^{12}	Ref.
				Type	Length [m]							
QCL	–	WM-2f	4.56	MP	–	–	–	CO	900	0.44 ppb	–	[65]
QCL	100	–	4.6	Herriott	5	Thermopile	–	CO	1	2 ppb	–	[70]
DFB	–	WM	2.04	Herriott	20	–	–	CO_2	0.06	62 ppb	–	[71]
DFB	11.2	WM-2f	2.73	HWG	0.8	TEC-MCT	–	CO_2	160	3 ppm	–	[72]
CW-TEC-DFB- ICL	4	WM-2f	3.559	Dense MP (BP: 7.6 cm)	3.75	TEC-MCT	200	Formaldehyde (CH_2O)	1	6 ppb	0.4	[73]
CW-TEC-DFB- ICL	3.8	–	3.483	Dense MP	50	TEC-PV-MCT	200	CH_2O	300	260 ppt	0.03	[74]
ICL	–	WM-2f	3.599	Dense MP (BP 7.6 cm	3.7	MCT	150	CH_2O	140	1.5 ppb	–	[75]
External cavity- QCL	<87	–	7.97	–	–	MCT	50	Water (H_2O)	1	31 ppm	–	[56]
DFB-QCL	120	WM and 2f	7.709	Herriott	76	TEC-PV-MCT	100	H_2O	2	11 ppm	0.003	[56]
DFB	–	WM	1.382	Direct	0.3	–	–	H_2O	0.27	0.89 ppm	–	[71]
DFB	11.2	WM-2f	2.73	HWG	0.8	TEC-MCT	–	H_2O	160	180 ppm	–	[72]
Tm:YAP	10^3	–	1.912	MP	1	InGaAs	–	H_2O	–	10 ppb (Conc. Res.)	0.1	[76]
DFB	5–11	–	2.476	Herriott	33	TEC-MCZT	–	Hydrogen fluoride (HF)	600	2.3 ppt	0.04	[77]
–	–	WM and 2f	7.8125	White MP (B.P. = 1.5 m)	127	–	0.4	Nitrous acid (HNO_2)	1800	300 ppt	–	[78]
External cavity- QCL	<87	–	7.965	–	–	MCT	50	Nitrous oxide (N_2O)	1	0.9 ppb	–	[56]
QCL	–	WM and 2f	7.8	MP (B.P. = 16.9 cm)	57.6	–	200	N_2O	1	2.6 ppb	–	[54]
DFB-QCL	120	WM and 2f	7.7098	Herriott	76	TEC-PV-MCT	80	N_2O	2	1.7 ppb	0.003	[58]
DFB	0.5	–	2.2005	–	0.142	InGaAs	–	Ammonia (NH_3)	0.08	70 ppm	42	[79]
Dual comb	0.2	–	1.4–1.7	Open path	100	InGaAs	–	NH_3	900	10 ppb	–	[80]
QCL	–	–	9.06	Herriott MP (BP: 70 cm)	30–60	TEC-MCT	–	NH_3	0.1	0.15 ppb	–	[81]
DFB	–	–	1.532	HWG	3	–	–	NH_3	6	7–14 ppm	–	[82]
			1.532		36			NH_3	30	0.2 ppm	–	[83]

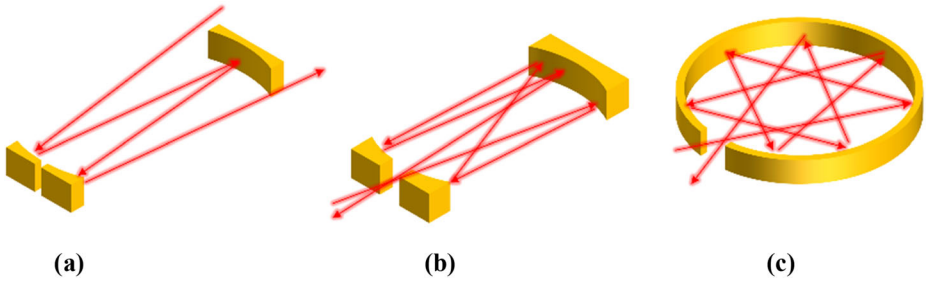

Figure 2. Different multipass gas cells configuration. a) White cell, b) Herriot, and c) circular multipass cell. The red arrows depict the direction of the light propagation, and the golden parts represent the mirrors.

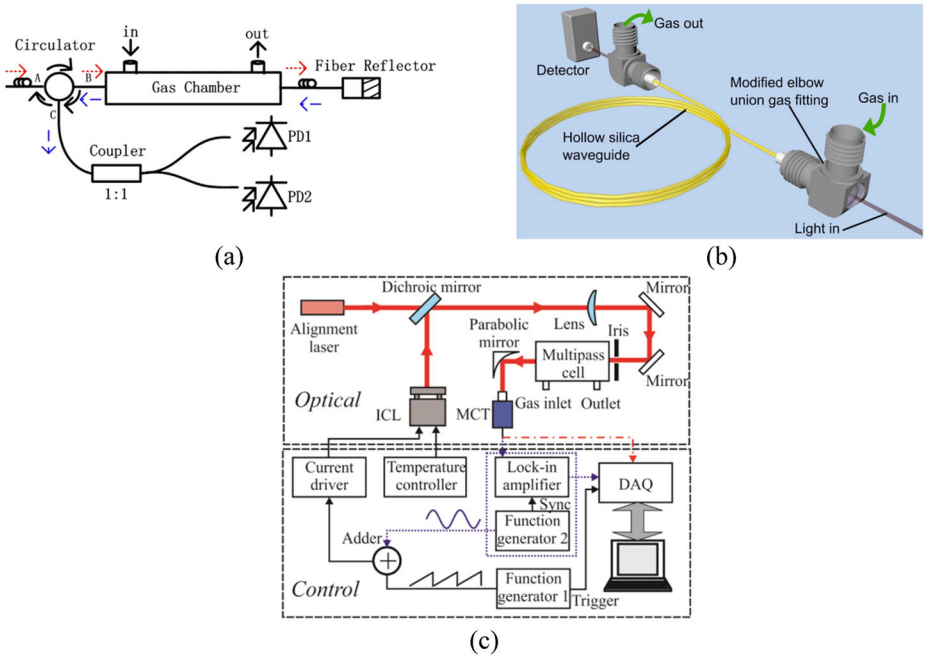

Figure 3. a) Schematic of the fiber reflector based round-trip structure. Reproduced with permission.[110] Copyright 2017, Elsevier. b) Gas sensing setup using HWG with special fittings for light coupling and gas flow. Reproduced with permission.[60] Copyright 2016, The Optical Society. c) Schematic of gas sensor system based on wavelength modulated laser, multipass cell in addition to alignment laser. Reproduced with permission.[74] Copyright 2015, The Optical Society.

two seed lasers, the output could be also tunable in the mid-IR region.

Chirped laser dispersion spectroscopy (CLaDS) is a less popular method based on probing the molecular dispersion of gas using two chirped lasers of different lasers. Due to dispersion, a difference in propagation time leads to a change in frequency spacing which can be further detected.[64] Measuring the phase variation instead of intensity fluctuations makes it immune to fluctuations in signal amplitude.[94]

Gas Cells: To achieve smaller detection limits, there is a need for multiplying the interaction length with the gas for a given volume. This can be accomplished using multipass gas cells, where the light bounces forth and back many times using high reflectivity mirrors. The most popular multipass cells are the White cell,[95] Herriott cell,[96] astigmatic Herriott cell,[97] and the circular gas cell.[98] The architectures of these cells are schematically depicted in **Figure 2**. A reflector can be added at the light output from the multipass cell to double the path length as depicted in **Figure 3**a, whereas a circulator/coupler should be used in the light input path. It is important to mention that increasing the path length dramatically limits the measurement dynamic range (i.e., the highest measurable gas concentration). This effect can be overcome by using a cell with two different paths.[46] Also, an additional reference path can provide better measurement reproducibility and less sensitivity to temperature.[99,100] An integrating sphere was reported to be used in gas sensing,[40,59,101] while it is not widely used due to its high losses compared to gas cells with metallic mirrors.

The use of a metallic hollow waveguide (HWG) is an alternative approach for increasing the path length using a small gas volume, compared to the multipass gas cells, and accordingly has a faster response time.[102] A setup for gas sensing using metallic HWG is depicted in Figure 3b. However, this method may induce larger losses due to the increased number of

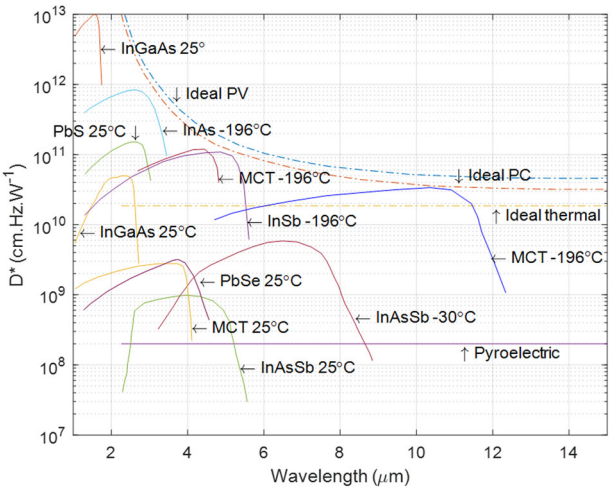

Figure 4. Specific detectivity of different detectors versus the wavelength of operation. PC denotes photoconductive and PV denotes photovoltaic. Data adapted from refs. [44, 112, 114, 115].

reflections of the light in the HWG, which is also filled with the gas under test.[103,104] Thus, the multipass cells have a better detection limit due to the smaller number of light reflections. HWGs can be integrated on a substrate leading to compact gas cells[105] or using 3D printing technology.

The cavity enhancement technique is another method for increasing the interaction path length by placing the gas inside an optical cavity. The effective path length is enhanced by $2F/\pi$[106] where F is the cavity Finesse, defined as the ratio between the cavity's full spectral range and full wave half maximum (FWHM). For mirrors of high reflectivity, the Finesse (F) is approximated to $\pi/(1-R_m)$, where R_m is the mirror reflectivity. Enhancements of hundreds of thousands could be achieved using mirrors of high reflectivity ($R \approx 99.999\%$).[32] This gain is achieved by locking the laser wavelength to the cavity resonance and the laser linewidth is well below the cavity mode width.[106–109]

Optical Detectors: Optical detectors in general can be classified into photon (quantum) detectors and thermal detectors. Quantum detectors can detect photons whose energy is greater than the bandgap energy of the semiconductor. This bandgap corresponds to the cut-off wavelength of the detector. By contrast, thermal detectors are able to detect light due to changes in temperature through the absorption of light.[44] They are characterized by a nearly flat and wide spectral response while suffering from higher noise and a slower response time compared to semiconductor-based detectors.

The specific detectivity D^* of the different detectors as a function of wavelength is depicted in **Figure 4**. The wavelength detectors such as InAs, InGaAs, and PbS are examples of quantum detectors while pyroelectric materials are an example of thermal detectors. The theoretical limits of D^* for all these detectors are represented by the dashed line. These limits correspond to the shot noise due to only the background thermal radiation, which is unavoidable.

In the case of near infrared (NIR), for wavelengths ranging from 1 to 1.7 μm, indium gallium arsenide (InGaAs) (peak responsivity at 1.7 μm) at room temperature can be considered as a highly sensitive detector and a popular choice.[111] For the wavelength range from 1 to 2.5 μm, extended InGaAs (peak responsivity at 2.3 μm) or lead sulfide (PbS) at room temperature are preferred. For better sensitivity, the nitrogen-cooled indium arsenide (InAs) can be used. In case of mid infrared MIR for the wavelength range of less than 5 μm, nitrogen-cooled indium antimonide (InSb) and nitrogen-cooled mercury cadmium telluride (MCT) are the preferred choices. For the wavelength range from 7.7 to 14 μm, cooled MCT is the better choice.[16,111,112] MCT is likely to remain unchallenged for its high performance in long wavelength infrared LWIR for the next few years.[113]

Theoretically, shot noise is the quantum limit of sensitivity of the optical detectors.[116] In practice, there are other noise sources affecting these systems such as laser source noise and optical fringes. The effect of laser source noise can be reduced by 1) increasing the absorbed signal by increasing the interaction length L using a cavity or a multipass cell, and 2) modulating the wavelength of the laser to operate away from the flicker noise due to laser power fluctuations.[32] TLS is also often limited by optical fringes rather than the theoretical detection limit of the detector.[32] These fringes arise from the parasitic Fabry–Pérot cavity introduced into the system by the different components such as the laser source, the detector, the optical windows and the collimation optics. These fringes are the main contributors to background noise.[117] Various methods have been described in the literature for suppressing the fringes such as wedging of the optical components,[47] antireflective coating for suppressing the Fabry–Pérot effect, dithering/mechanical vibration of the optical components to vary the cavity length, double-tone modulation[117] and using neural algorithms.[118] TLS is also affected by light intensity fluctuations and baseline-fitting errors, which can also be minimized by modulation.[63] Modulation relies on imposing a sinusoidal current component at a high frequency f_m to the slower ramp laser current (ramp current is responsible for spectrum scanning). Thus, the laser wavenumber equation is given as[119,120]

$$\nu_l(t) = \bar{\nu}_l(t) + \nu_a \cos\left(2\pi f_m t\right) \tag{9}$$

where $\bar{\nu}_l(t)$ is the corresponding ramp wavenumber function and ν_a is the corresponding modulation wavenumber amplitude. Substituting the above equation in Beer–Lambert's law for an interaction with a gas of small absorption ($\alpha(\nu)l \ll 1$), the transmitted power is given by

$$P(t) \sim P_o(t)\left(1-\alpha(\nu)l\right) = P_o(t)\left(1-\alpha\left(\bar{\nu}_l(t) + \nu_a \cos\left(2\pi f_m t\right)\right)l\right) \tag{10}$$

where P_o is the laser power. The imposed harmonic component leads to a periodic signal for the detected power, which can be further decomposed by the Fourier series into its harmonic components including the second harmonic $2f_m$ that is away from the flicker noise. Another advantage of this method is the ability to have a free calibration method independent of the laser power since the ratio between different harmonics is independent of the laser power but dependent on the gas absorption.[120] A schematic of a setup exploiting the wavelength modulation is depicted in Figure 3c. Based on that, TLS with modulation is classified into frequency modulation spectroscopy (FMS) and

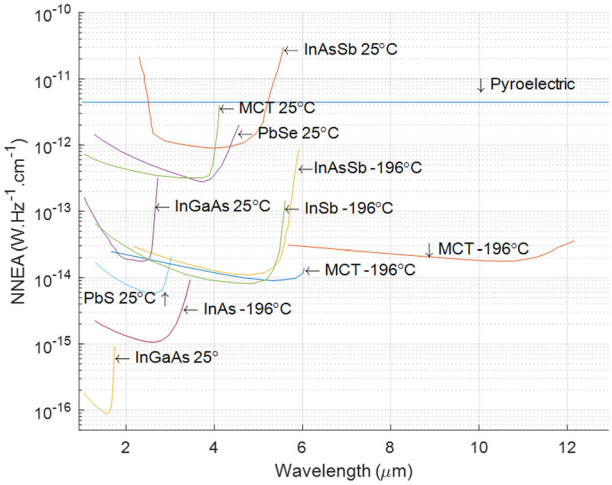

Figure 5. NNEA of DAS of different detectors (detector diameter = 1 mm and path length = 1 m).

wavelength modulation spectroscopy (WMS).[121,122] The modulation frequency in WMS is smaller than the spectral width of the gas absorption line (a few kHz to a few MHz) whereas it is equal to or larger in the case of FMS (>100 MHz). The modulation index is higher in WMS than in FMS.[121]

NNEA: NNEA coefficient is a common figure of merit in the PAS. NNEA is the product of the normalized minimum absorption coefficient (absorption coefficient normalized with respect to the measurement time) and the laser power so it is dependent only on the detector characteristics. Thus, one can use it to compare different PA systems. Trying to define such parameters in the DAS, in the case of a shot noise limited system leads to a power-dependent NNEA, which cannot be used as a comparison figure of merit. However, in some circumstances, the detection limit in the DAS originates from the thermal noise of the detector instead of the shot noise, for example in an uncooled detector, with a large detector area or small laser power. The thermal noise increases with the optical detector area A_d and can be related to the specific detectivity in Figure 4. Returning to Equation (6) and knowing that NEP = $\sqrt{A_d}/D^*$,[44] the corresponding NNEA can be given by

$$\mathrm{NNEA_{DAS}} = \frac{\sqrt{A_d}}{D^* l} \tag{11}$$

In the above equation, the NNEA is path length and area dependent but is independent of the optical power. The NNEA curves of the DAS, of different detector types, are plotted in **Figure 5** using Equation (11) and the data in Figure 4. The curves correspond to detectors of diameter of 1 mm and gas cell path length of 1 m with no propagation losses and assuming that the system is thermal-noise limited. For different detector areas, one multiplies the NNEA curves by $\sqrt{A_d}$, where A_d is in (mm)^2. For such curves, the NNEA is independent of the laser power and increasing the source power directly enhances the sensitivity. Nitrogen-cooled MCT detectors have the best sensitivity in the MIR range while the InGaAs detector has good performance in the NIR range (1.2 to 3 μm) as does the PbS. The sensitivity of the DAS degrades for higher wavelengths in the case of a thermal-noise-limited system. In the case of different path lengths, one could easily divide the curves by the new length in meters. These curves will be used later to compare the DAS and PAS. For different detector diameters, one directly multiplies the curves by $\sqrt{A_d}$ where A_d is in (mm)^2.

2.2. Laser-Based PAS

A simple illustration of the PAS mechanism is depicted in **Figure 6**. The system consists of an excitation light source, which could be a laser, light emitting diode (LED) or even a white light source. The light is coupled into an acoustic cell containing a gas that absorbs optical power at a wavelength aligned with the excitation wavelength. Consequently the molecules are excited to a higher energy level. After that, the molecules relax the energy in a nonradiative form (i.e., kinetic or translational energy) via inelastic collisions. Such a process occurs within a time denoted as the relaxation time τ_R. This leads to a rise in the local temperature T, which corresponds directly to a rise in the local pressure P. The heat energy then transfers to the walls of the cell in a response time τ_H. Introducing an amplitude modulation of the excitation light leads to variations in the pressure versus the time generating an acoustic wave. The acoustic wave propagates inside the PA cell and can be detected by a microphone. The sensitivity of the PA sensors strongly depends on the geometry of the PA cell, and can be improved further by operating at its resonance frequency.[123,124] Most of the cells described in the literature are used in conjunction with cantilevers that have a cylindrical form whose length and diameter typically range from 1 to 20 mm.

2.2.1. Theoretical Fundamental Detection Limit of Laser-Based PAS

In the PAS, a laser of a given wavelength λ and power P_o is modulated with a repetition rate $\omega = 2\pi f$ (rad s^{-1}). The modulated laser is coupled into a photoacoustic cell with an illumination area A_{cell} and cell length l containing a gas with an absorption coefficient α. The PA cell comprises the cantilever for acoustic wave detection. As mentioned before, we are limiting our analysis to cantilevers as an example of high-performance microphones. The cantilever motion can be detected using an interferometer to achieve high dynamic range and sensitivity. The deflection of the cantilever x produces fringes at the interferometer output, which corresponds to the magnitude of beam deflection.[125] The cantilever dimensions are $b_b \times l_b \times t_b$ (width × length × thickness). By solving a set of equations, namely the gas law equation, the heat transfer rate equation, the first law of thermodynamics and the cantilever second-order differential equation, one can find a relation between the absorbed power $P_o \alpha l$ and beam deflection x (for a nonresonant PA cell):[126]

$$x = \frac{b_b l_b (\kappa - 1)}{A_{cell}} \alpha P_o \frac{1}{k\sqrt{\left(1 - \frac{\omega^2}{\omega_o^2}\right)^2 + \left(\frac{\omega}{Q\omega_o}\right)^2}} \frac{\tau_H}{\sqrt{1 + (\omega\tau_H)^2}} \times \frac{\omega\tau_L}{\sqrt{1 + (\omega\tau_L)^2}} \frac{1}{\sqrt{1 + (\omega\tau_R)^2}} \tag{12}$$

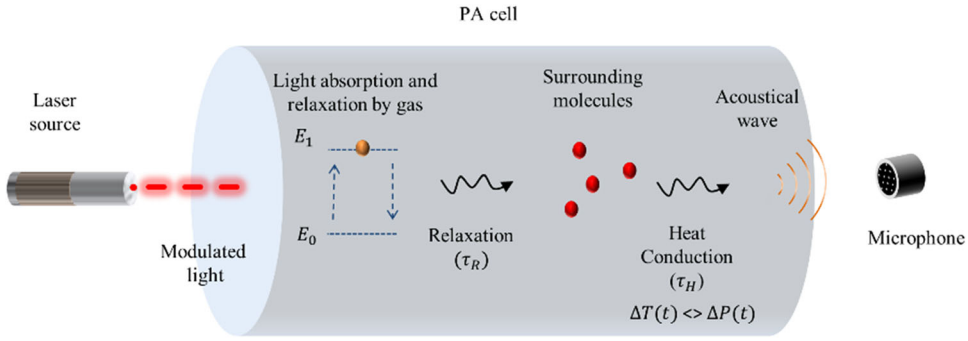

Figure 6. Illustration of the PAS mechanisms including light absorption, vibrational relaxation, heat conduction, and propagation of acoustical waves.

where ω_o, k, and Q are the beam resonance angular frequency, stiffness, and quality factor, respectively, and κ is the ratio of the specific heat capacity at a constant pressure to the specific heat capacity at a constant volume (for air, $\kappa = 1.4$ at $T = 300$ K[127]). The heat conduction effect has a first order, low-pass, filter response with a response time, τ_H. The leakage between the PA cell and the interferometer chamber, due to the pressure difference, is represented by a first-order, high-pass, filter of time constant, τ_L. The gas relaxation time response, which is the time of heat release due to the nonradiative relaxation of the excited molecules, is modeled by a first-order, low-pass, filter with a time constant, τ_R. The heat conduction of the surrounding/diluting gas affects the response of the detected signal. It also can affect the PA detection limit (e.g., carbon dioxide (CO_2) where the detection limit differs for argon or nitrogen[128]). The model assumes that the gas is a continuous medium, which can be expressed by macroscopic quantities such as density, pressure and temperature. The validity of using the continuum model as a function of the density of gas molecules for different cases.[129]

The above equation can be simplified by making use of the following considerations. 1) The modulation frequency, ω, can be operated in the nonresonant mode of the cantilever ($\omega < 0.25\ \omega_o$) as the Brownian noise is amplified with the PA signal around the resonance and, thus, there is no enhancement in the signal to noise ratio around the resonance.[1,30] Also, nonresonance operation is not compatible with the operation of FTIR spectrometers for which a wide range of modulation frequencies with a flat response is required. 2) The thermal response time increases dramatically with increasing the cell volume. For a cylindrical PA cell, the response time is given by $\tau_H \approx \frac{\rho_g c_v r^2}{\Lambda}$[126], where Λ is the thermal conductivity, ρ_g is the gas density, c_v is the heat capacity at constant volume, and r is the cell radius. For air, $\rho_g = 1.177$ kg m^{-3}, $c_v = 718$ J kg^{-1} K^{-1}, and $\Lambda = 0.0262$ W K^{-1} m^{-1} at $T = 300$ K and a cell of radius $r > 1$ mm. In this case the heat conduction response time τ_H is greater than 0.1 s. To reduce acoustical noise, the repetition rate should be greater than 100 Hz ($\omega^2 \tau_H^2 \gg 1$), then, the heat response time can be approximated by ω^{-1}. 3) The gas relaxation time is dependent on the gas type and the gas mixture. Its value ranges from ms to ns.[130–135] In addition, it is inversely proportional to the gas pressure. This makes the PA signal dependent on the gas sample conditions. The best performance of the system is achieved for gases with a low relaxation time and minimum air leakage from the cell. Based on the discussion above, the displacement relation becomes[126]

$$x = \frac{b_b l_b (\kappa - 1)}{A_{cell} k \omega} \alpha P_o \tag{13}$$

Note that the response is apparently independent of the path length. Undesired photoacoustic signals, generated by the windows installed in the PA cell, can be reduced by increasing the cell length so that the signal is spread over a larger volume.[30] One can define the gas cell constant, as the ratio of cantilever deflection to the product of the absorption coefficient and power. This is given by

$$C = \frac{b_b l_b (\kappa - 1)}{A_{cell} k \omega} = \frac{(\kappa - 1)}{A_{cell} \rho_b t_b \omega_o^2 \omega} \quad \left(\text{m}^2\ \text{W}^{-1}\right) \tag{14}$$

where ρ_b is the cantilever density. Thus, a noisy PA signal is given by

$$x = C P_o \alpha + \Delta x_n \sqrt{\Delta f} \tag{15}$$

where Δx_n represents the noise normalized to the square root of the measurement bandwidth. Then the signal-to-noise ratio (SNR) is given by

$$\text{SNR} = \frac{P_o \alpha C}{\Delta x_n \sqrt{\Delta f}} \tag{16}$$

The minimum detectable absorption coefficient, defined as the detectable absorption coefficient, when the SNR is unity, normalized to the square root of the measurement bandwidth, is given by

$$\alpha_{\min \text{PA}} = \frac{\alpha}{\text{SNR}\ \sqrt{\Delta f}} = \frac{\Delta x_n}{P_o C} \tag{17}$$

Then, the NNEA is given by

$$\text{NNEA}_{\text{PAS}} = \alpha_{\min \text{PA}}\ P_o = \frac{\Delta x_n}{C} \tag{18}$$

It is clear that the NNEA in the PAS is independent of the laser power and the measurement time but depends on the cell

response and noise. The encountered noise types are acoustical noise, Brownian noise, source fluctuation noise, vibrational (or acceleration) noise, light back-action on the cantilever (fluctuation in radiation pressure),[136] and thermal and shot noise due to the optical detector used in the beam deflection measurement. For an ideally sealed cell, the sum of dominant sources of noise is given by

$$\Delta x_{\mathrm{n}}^2 = \langle x_{\mathrm{Bn}}^2 \rangle + \langle x_{\mathrm{Sn}}^2 \rangle + \langle x_{\mathrm{ban}}^2 \rangle \tag{19}$$

where x_{Bn}, x_{Sn}, and x_{ban} represent the Brownian noise, shot noise (laser source of the cantilever detection interferometer), and back-action noise, respectively. The symbols $\langle\ \rangle$ indicate the statistical average. Increasing the laser power, P_{b}, leads to decreasing the shot noise but increasing the back-action noise. An optimum value of the power for nonresonant operation, is given by[136]

$$P_{\mathrm{b}} = \frac{k_{\mathrm{b}} c \lambda}{8\pi} \tag{20}$$

where c is the speed of the light. In this case, the total displacement noise can be given by[136]

$$\Delta x_{\mathrm{n}}^2 = \left(\frac{4 K_{\mathrm{B}} T_{\mathrm{BG}}}{\omega_{\mathrm{o}} Q} + \frac{2h}{\pi} \right) \frac{\Delta f}{k} \tag{21}$$

The Brownian noise term is the dominant term as long as $f_{\mathrm{o}} Q \ll \frac{K_{\mathrm{B}} T_{\mathrm{BG}}}{h} \approx 6 \times 10^{12}$. This condition is practically satisfied even at high frequencies. The stiffness equation is given by[137]

$$k = \frac{\lambda_{\mathrm{n}}^4}{12} \frac{t_{\mathrm{b}}^3}{l_{\mathrm{b}}^3} b_{\mathrm{b}} E \tag{22}$$

where E is the Young's modulus and λ_{n} is the mode Eigenvalue (for first mode: $\lambda_1 = 1.875$). In the viscous regime (air pressure is in the vicinity of atmospheric pressure), by modeling the beam as a string of spherical beads, the quality factor can be given by[137]

$$Q = \frac{\lambda_{\mathrm{n}}^2 t_{\mathrm{b}}^2 \sqrt{E \rho_{\mathrm{b}}}}{12\sqrt{3}\pi \mu l_{\mathrm{b}} \left(1 + b_{\mathrm{b}} \sqrt{\frac{\rho_{\mathrm{g}} \omega}{2\mu}} \right)} \tag{23}$$

where μ is the viscosity of the surrounding fluid (for air: $\mu = 18.6$ μPa s and for nitrogen: $\mu = 17.9$ μPa s at 300 K and 1 atm.[138]). In view of Equation (17) and (21)–(23), α_{min} is given by

$$\alpha_{\mathrm{min\,PA}} = \frac{4\omega A_{\mathrm{cell}}}{P_{\mathrm{o}} (\kappa - 1)} \sqrt{\frac{3\sqrt{3} K_{\mathrm{B}} T_{\mathrm{BG}}\ \pi \mu \omega_{\mathrm{o}}}{\lambda_{\mathrm{n}}^2 t_{\mathrm{b}}} \left(\frac{1}{b_{\mathrm{b}}} + \sqrt{\frac{\rho_{\mathrm{g}} \omega}{2\mu}} \right) \sqrt{\frac{\rho_{\mathrm{b}}}{E}}} \tag{24}$$

For a beam diameter in the range of few mms or larger ($f b_{\mathrm{b}}^2 \gg \frac{\mu}{\pi \rho_{\mathrm{g}}} \approx 5.1\ (\mathrm{mm})^2\ \mathrm{s}^{-1}$), Equation (24) can be approximated by

$$\alpha_{\mathrm{min\,PA}} = \frac{13.6}{P_{\mathrm{o}}} \left(\frac{\omega}{\omega_{\mathrm{o}}} \right)^{1.25} \omega_{\mathrm{o}}^{1.75}\ \theta_{\mathrm{PA}} \Gamma_{\mathrm{g}} \tag{25}$$

where θ_{PA} is frequency independent but depends on the component dimensions: the cantilever thickness and the cell area. It is given by

$$\theta_{\mathrm{PA}} = A_{\mathrm{cell}} \sqrt{\frac{1}{\lambda_{\mathrm{n}}^2 t_{\mathrm{b}}} \sqrt{\frac{\rho_{\mathrm{b}}}{E}}} \tag{26}$$

and

$$\Gamma_{\mathrm{g}} = \frac{\sqrt{K_{\mathrm{B}} T_{\mathrm{BG}}\ \sqrt{\rho_{\mathrm{g}} \mu}}}{(\kappa - 1)} \tag{27}$$

The θ_{PA} of published designs ranges from 0.4×10^{-6} mHz$^{-0.5}$ (very small A_{cell}) to nearly 800×10^{-6}mHz$^{-0.5}$ (thick cantilever) (see **Table 2**). From the above equation, one can see that the detection limit depends on different parameters which correspond to different system components as follows: 1) ratio of the modulation frequency to the cantilever resonance frequency, cantilever resonance frequency, cantilever thickness, and cantilever specific stiffness E/ρ_{b}, 2) laser power, 3) cell area, and 4) the density of the gas inside.

Decreasing the ratio of $\omega/\omega_{\mathrm{o}}$ by 10 dB enhances the detection limit by 12.5 dB. In addition, the detection limit is enhanced by decreasing the cantilever resonance. Using typical values of the cell diameter, the modulation frequency and the cantilever thickness in the literature (see Table 2), one can draw a color map of NNEA or ($\alpha_{\mathrm{min\,PA}} P_{\mathrm{o}}$) for different $\omega/\omega_{\mathrm{o}}$ and resonance frequencies f_{o} in the case of unity θ_{PA} as shown in **Figure 7**a. For different θ_{PA}, one simply multiplies the map by the corresponding value.

Increasing the cantilever thickness enhances performance. However, increasing the thickness by 10 dB increases the stiffness by 30 dB according to Equation (22), which increases the optimum laser power by 30 dB according to Equation (20). Thus, increasing the thickness is not practical. The higher the E/ρ_{b} is, the better the sensitivity. NNEA is also plotted in Figure 7b for different cantilever thicknesses and different E/ρ_{b} ($f_{\mathrm{o}} = 500$ Hz, $\omega/\ \omega_{\mathrm{o}} = 0.2$ and the cell diameter equals 5 mm). It is apparent from this figure that silicon has high specific strength compared to various metals and polymers.

The detection limit is enhanced linearly with the source power,[28] which is an advantage compared to the DAS. Decreasing the cell area enhances the system's sensitivity unless it affects the flow of the gas into the cavity. Finally, it is apparent from Equation (25) that there is no dependence on the wavelength of operation as compared to the DAS.

2.2.2. Survey of Laser-Based PAS Systems

Excitation Sources: Erbium-doped ring lasers,[139] DFB,[140,141] CO_2 lasers,[142] visible LEDs,[143] IR LEDs,[144] and THz diodes[145,146] are among the sources used with PA cells equipped with cantilevers. Lasers are more common than LEDs due to their higher optical power. To enhance the sensitivity of such systems, optical amplifiers such as Erbium-doped fiber amplifiers have been used.[139] Another type of source is a blackbody emitter followed by an IR filter at the corresponding absorption wavelength of the gas. Blackbody sources are either

Table 2. Summary of CEPAS systems. Light sources are indicated with their corresponding coupled power if reported. Units are specified in the first row. BB stands for black body.

Excitation source	Modulation type	Wavelength [μm]	Cantilever			Detection method	NNEA [cm^{-1} W $Hz^{-0.5}$]	Cell dimensions (radius [mm]/ length [mm])	$\theta_{PA} \times 10^6$ [m $Hz^{-0.5}$]	Gas	Detection limit/ average time	Ref.
			Material	Dimensions (L [mm] × W [mm] × t [μm])	f_r [Hz]/operation mode							
1 W DFB-EDFA	WM-2f	1.576	Stainless	1.7 × 0.6 × 10	–	WL-FPI	–	–	–	Hydrogen sulfide (H_2S)	30 ppb/10 s	[140]
EDF ring laser - EDFA	WM-2f	1.523	–	2.1 × 1 × 10	–	FPI	–	–	–	Ammonia (NH_3)	3 ppb	[139]
1 W DFB-EDFA	WM-2f	1.533	Stainless	2 × 0.5 × 10	2000	WL-FPI	1.1×10^{-9}	2/120	30	Acetylene (C_2H_2)	0.5 ppb/5 s	[151]
14 mW DFB	–	1.529	Silicon	0.5 × 0.1 × 1	5000/off	Laser and quadrant detector	1.2×10^{-7}	/ 3		C_2H_2	1.3×10^{13} molecule cm^{-3}/1 s	[152]
23 mW C-band	–	1.530	–	2.8 × 1.8 × 30	914/at	L-FPI	–	0.3/2	–	C_2H_2	330 ppb/1 s	[181]
23 mW C-band	WM-2f	1.53	Borosilicate	0.3 × 0.3 × 30	1196/at	L-FPI	7.7×10^{-10}	0.3/2	0.4	C_2H_2	15 ppb/0.3 s	[149]
12 mW L-band	WM-2f	1.572	–	0.3 × 0.3 × 30	/off	FPI	1.3×10^{-9}	0.3/11	–	C_2H_2	25ppb/1 s	[177]
7.5 mW DFB	WM-2f	1.53	Silicon	–	–	MI	1.75×10^{-12}	2/95 inside a cavity	–	C_2H_2	24 ppt/100s	[184]
1 W DFB-EDFA	WM-2f	1.53	Stainless	2.51 × 1 × 10	1400/at	WL-FPI	4.2×10^{-10}	4/120	120	C_2H_2	27 ppt/200 s	[194]
EDF	WM-2f	1.53	Silicon	–	–	FPI	1.72×10^{-9}	–	–	C_2H_2	200 ppt/60 s	[195]
BB + filter	–	3.07	–	5 × 1.2 × 10	–	Interferometer	–	–	–	C_2H_2	8 ppb/80 s	[196]
DFB		1.53	Silicon	5 × 1.2 × 10		Vibration meter	–	2/95	23	C_2H_2	270 ppb	[197]
(0.8–3 mW/each) four DFB	WM and FDM	1.534	Silicon	6 × 1.5 × 10	300/off	MI	3.6×10^{-9}	3/115	51	C_2H_2	1.5ppm/2.6 s	[153]
(0.8–3 mW/each) four DFB	WM and FDM	1.567	Silicon	6 × 1.5 × 10	300/off	MI	3.4×10^{-9}	3/115	51	Carbon monoxide (CO)	250 ppm/2.6 s	[153]
DFB		1.568	Silicon	5 × 1.2 × 10		Vibration meter	–	2/95	23	CO	120 ppb	[197]
(10 mW) DFB	Chopper	1.568	Silicon	5 × 1.2 × 10	40/off	MI	–	2/95	23	CO diluted in N_2/SF_6	3.63/9.88 ppm	[198]
7.8 mW DFB	WM-2f	1.392	Silicon	L-shaped (0.8 and 0.3 × 0.2 and 0.12 × 10)	3098	L-FPI	1.08×10^{-7}	0.45/4.5	1	Water (H_2O)	–	[141]
9 mW DFB	WM-2f	1.396	Polyvinylidene fluoride	25 × 13.2 × 200	–	Piezoelectric	2.4×10^{-7}	2.5/30	783	H_2O	40 ppm	[175]
QCL	WM-2f	4.527	–	–	–	–	8×10^{-9}	–	–	Carbon dioxide isotope ($^{14}CO_2$)	30 ppt/9 min	[199]

(*Continued*)

Table 2. (Continued).

Excitation source	Modulation type	Wavelength [μm]	Cantilever			Detection method	NNEA [cm^{-1} W $Hz^{-0.5}$]	Cell dimensions (radius [mm]/ length [mm])	$\theta_{PA} \times 10^6$ [m $Hz^{-0.5}$]	Gas	Detection limit/ average time	Ref.
			Material	Dimensions (L [mm] × W [mm] × t [μm])	f_r [Hz]/operation mode							
Two DFB -EDFA	FDM	–	–	–	–	–	3.4× 10^{-10} (3)		–	Carbon dioxide (CO_2)	–	[200]
BB + filter	–	4.25	Silicon-coated with PZT material	2 × 2 × 10	–	Piezoelectric	-	4/15	91	CO_2	330 ppm	[148]
DFB	WM-2f	2	–	–	–	FPI	-	–	–	CO_2	44 ppb	[201]
4.9 mW QCL	WM-2f	4.344	Silicon coated with PZT material	×0.79 × 3.9	60 kHz/	Piezoelectric	3 × 10^{-7}	2.3 mm^3 Integrated Silicon cell	–	CO_2	900 ppb/7 s	[202]
600 mW DFB		1.572	Silicon	6 × 2 × 10	350/off	MI	7.32 × 10^{-10}	1.5/61	13	CO_2	0.23 ppm/75 s	[128]
30 μW LED	AM	4.2	Stainless	10 × 3 ×10	1070/off	MI	–	5/42	187	CO_2	11 ppm/1 s	[144]
5 mW QCL	WM-2f	14.8	–	–	–	–	–	2/90		Benzene (C_6H_6)	1 ppb	[203]
300 mW CO_2 laser	–	9.676	Multilayer graphene	6 × 3 × 50	–	Laser and quadrant detector	–	3/107	15	Methanol (CH_4O)	330 ppb	[142]
(0.17–1 W) CO_2 laser	–	9.24	Mica	Circular (r = 6.5 mm, t = 10 μm)	275/at	Laser and quadrant detector	–	3/145	–	Acetone (C_3H_6O)	24.8 ppm/0.3 s	[188]
		10.24							–	Acetic acid (CH_3COOH)	0.54 ppm/0.3 s	
		9.5							–	Methanol (CH_4O)	0.8 ppm/0.3 s	
		9.5	Mica	4 × 2 × 1	581/at		–		172	CH_4O	1.8 ppm/0.3 s	
		9.5	Multilayer graphene	5 × 7 × 1	252/at		–		104	CH_4O	0.9 ppm/0.3 s	
1 W OPO (2.7–3.4 μm)	WM-2f	3.289	Silicon	–	/off	MI	–	–	–	Methane isotope ($^{14}CH_4$)	3 ppb	[204]
(0.8–3 mW/each) four DFB	WM and FDM	1.62	Silicon	6 × 1.5 × 10	300/off	MI	1.4 × 10^{-9}	3/115	51	Methane (CH_4)	293.7 ppm/2.6 s	[153]
BB with filter	AM	3.3	Silicon	4 × 2 × 5	470/off	MI	–	–	–	CH_4	9.5 ppb/0.73 s € x_{rms} = 2pm	[125]
MEMS BB, + filter	AM	≈3.3	Silicon (two cantilevers)	6 × 4 × 10	–	MI	–	–	–	CH_4	0.5 ppm/5 s	[147]
1300 K BB	AM	–	Silicon	4 × 2 × 5	360–420	MI	–	5/100 + 1 m DA cell	200	CH_4	10 ppb/0.37 s	[178]

(*Continued*)

Table 2. (Continued).

Excitation source	Modulation type	Wavelength [μm]	Cantilever			Detection method	NNEA [cm^{-1} W $Hz^{-0.5}$]	Cell dimensions (radius [mm]/ length [mm])	$\theta_{PA} \times 10^6$ [m $Hz^{-0.5}$]	Gas	Detection limit/ average time	Ref.
			Material	Dimensions (L [mm] × W [mm] × t [μm])	f_r [Hz]/operation mode							
12 mW DFB	WM-2f	1.651	Silicon	2.2 × 0.6 × 10	–	WL-FPI	2.1×10^{-8}	0.5/2.2	1.4	CH_4	8.4 ppm/1 s	[205]
DFB	–	1.651	–	2.8 × 1×	1290/at	L-FPI	–	10/	–	CH_4	127 ppb/1000 s	[206]
20 mW DFB	WM-2f	1.651	–	Fiber	1150/off	WL-FPI	–	4/120	–	CH_4	9 ppb/500 s	[207]
1.8 mW ICL	WM-2f	3.356	Silicon-coated with PZT material	×0.79 × 3.9	60 kHz/	Piezoelectric	2.4×10^{-7}	2.3 mm^3 Integrated Silicon cell	–	CH_4	2.5 ppm/7 s	[202]
MIR LED	AM	–	Silicon	2.2 × 1 ×10	–	MI	–	1.2/8 + mm DA cell	8	CH_4	300 ppm/1 s	[186]
30 mW DFB	WM-2f	0.76	Silicon	6 × 2 × 10	–	MI	4.8×10^{-9}	1.5/6	–	Oxygen (O_2)	20 ppm	[208]
20 mW L-band	AM	1.6	Silicon	–	–	MI	–	3/100	–	Hydrogen sulfide (H_2S)	8 ppm/50 s	[183]
53 mW laser diode + EDFA	–	1.742	Silicon	–	–	MI	–	Multipass PA cell	–	Hydrochloric acid (HCL)	0.2/300 s	[209]
0.95 W OPO pumped by DFB	WM-2f	2.476	Silicon	–	–	MI	2.7×10^{-10}	2/95	–	Hydrofluoric acid (HF)	5 ppt/ 1 s	[33]
47 mW QCL	AM	5.637	Silicon	–	–	MI	7.32×10^{-10}	2/95	–	Formaldehyde (CH_2O)	0.901 ppb /14.3 s	[162]
	WM-2f						6.04×10^{-10}		–		0.623 ppb /28.5 s	
50 mW LED	AM	0.455	–	Fiber D = 125 μm, L = 8–10 mm	–	Fiber to detector	-	10 × 3 × 3 mm^3	–	Nitrogen dioxide (NO_2)	50 ppm	[143]
4.7 W Nd : YVO4	AM	0.532	Silicon	–	–	MI	2.6×10^{-10}	2/95	–	NO_2	50 ppt/1 s	[210]
<3.6 W laser diode	–	0.45	–	–	1858	WL-FPI	–	2/120	–	NO_2	1.26 ppb	[211]
100 mW LED	AM	0.44	Silicon	–	/off	MI	–	4/40	–	NO_2	1 ppb/1 s	[212]
150 μW MIR LED	AM	3.4	Stainless	10 × 3×10	1070/off	MI	–	5/42	–	Propane (C_3H_8)	6 ppm/1 s	[144]
5 μ W THz LED	AM	400 GHz	Silicon	7 × 2 ×10	280/at	MI	4.28×10^{-10}	5/50.8	141	Methyl cyanide ($C_2H_3N_1$) (15 mTorr)	$1.71 \times 10^{-5} cm^{-1}$/0.5 s	[145, 146]
5 mW QCL	WM	14.8	Silicon	–	/off	MI	–	–	–	Benzene (C_6H_6)	150 ppt/90 s	[213]

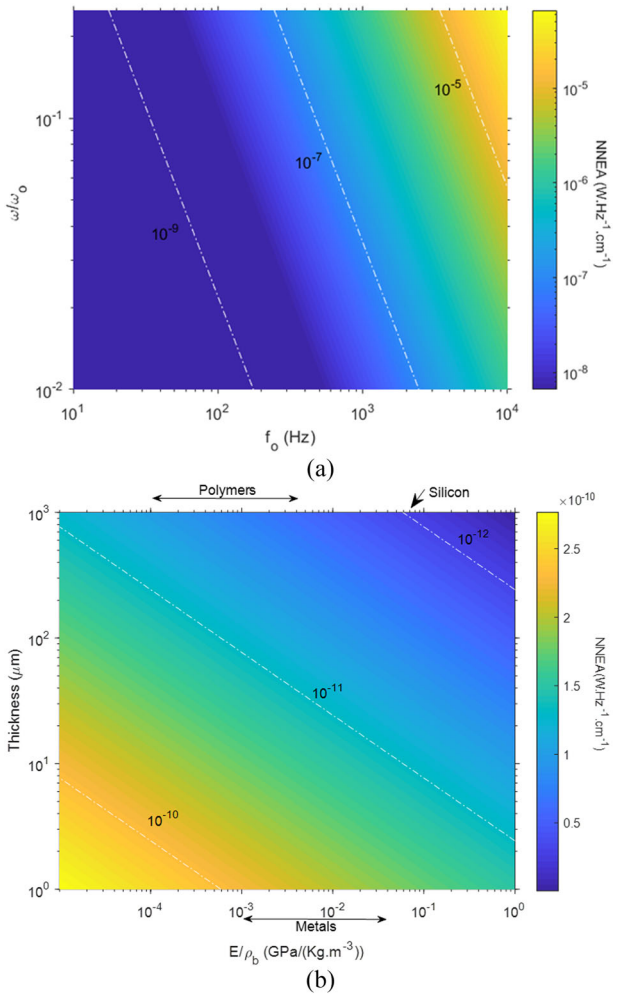

Figure 7. a) Color map of the NNEA versus ω/ω_o and resonance frequency f_o of the cantilever ($\theta_{PA} = 1$). b) Color map of the NNEA as function of stiffness and cantilever thickness (f_o = 500 Hz, ω/ω_o= 0.2 and cell diameter = 5 mm).

electrically amplitude modulated (EM) at low frequencies[140,147] or modulated using a mechanical chopper.[125] This technique is characterized by its simplicity but lack of power and the slow response time limit its electrically modulated frequency to less than 50 Hz,[148] and so laser sources are still superior.

In the case of the laser, it is more efficient to use wavelength modulation and detect the 2nd harmonic signal.[139,149] When using wavelength modulation, the PA signal is dependent on the wavelength-dependent losses, such as the absorption lines of the gases, not the losses introduced by the windows and the walls.[33,124] Compared to conventional sinusoidal modulation, triangular-shaped and quasi-square waves enhance the photoacoustic signal by factors of 1.12, 1.42, and 1.57, respectively.[150]

The modulation frequency can be off resonance for a flat response operation[128,140,151] or at resonance.[149,152] For the 2nd harmonic detection, the modulation frequency should be half the 2nd harmonic frequency. For multiple component analysis at the same time, multiple laser sources can be combined using frequency division multiplexing (where each laser is WM modulated at different frequency) and detected using the same PA detector.[153]

Acoustic Detector: Microphones used in the PAS can be capacitive (electret or condenser)[154,155] piezoelectric, quartz tuning forks,[156] cantilevers, polymer diaphragms,[157,158] and membranes. Recently, cantilevers have appeared as a strong candidate for PA detection with researchers taking advantage of the results from detailed studies and optimization of cantilevers used in atomic force microscopes. The motion of the cantilever is characterized by its high linearity and large dynamic range, which is larger than that of conventional membranes.[124–126,142,159] In addition to that, the limited sensitivity of the membrane cannot be improved by further decreases in the gap.[126] An experimental comparison of an electret microphone, a differential microphone and a cantilever demonstrated the superiority of the latter by two orders of magnitude over microphones.[126,160,161] NNEA in the order of 10^{-10}cm^{-1} W Hz$^{-0.5}$ can be achieved without using a resonant PA cell with a cantilever.[162] On the other hand, these values can be attained using an electret microphone with a resonant PA cell. For example, a differential Helmholtz resonator PA cell (resonance frequency: 320 Hz) equipped with electret microphones (sensitivity 100 mV Pa^{-1}) was reported to have an NNEA of 2.4×10^{-10} cm^{-1}W Hz$^{-0.5}$.[163] Recently,[164] described an NNEA of 2.4×10^{-10} cm^{-1}W Hz$^{-0.5}$ using T-cell based differential photoacoustic spectroscopy with a condenser microphone. Using a broadband Globar light source of 30 mW, detection limits of hundreds of ppb were achieved in case of carbon dioxide, acetylene, and water.

An alternative is to use a quartz tuning fork as a resonant transducer. It is characterized by its high-quality factor (can reach 8000 or even 18 000 at low pressure[165]) and its immunity to acoustical noise due to its high resonance frequency (32.8 kHz).[126] Acoustical resonance in conjunction with quartz can be used to improve the sensitivity.[124] It can also be used in conjunction with a high finesse cavity[166] or multipass cell[167] to further improve the sensitivity. The obtained NNEA values are around 10^{-10} cm^{-1}W Hz$^{-0.5}$.[165,168,169] Better sensitivity was reached by measuring methanol (CH_3OH) using a THz quantum cascade laser at 3.93 THz. The achieved NNEA was 3.75×10^{-11} cm^{-1}W Hz$^{-0.5}$.[170] However, using such a structure has drawbacks: 1) a precise adjustment of the modulation frequency is needed,[171] 2) it is incompatible with blackbody sources, which cannot be modulated with such a high frequency,[126] and 3) it cannot be used with scanning FTIR spectrometers due its limited bandwidth. A detailed review of QEPAS was recently published.[172] Thus, the focus of this review is on cantilever-based PAS.

For the cantilever-based microphone, different materials have been used such as silicon,[125] mica for highly corrosive chemicals,[173] stainless steel,[174] silica, borosilicate,[149] and polyvinylidene fluoride.[175] The process of fabricating cantilevers made from silicon.[176]

The higher the length to thickness ratio of the cantilever, the lower the stiffness of the beam and consequently, the higher its sensitivity. However, this makes the cantilever more fragile and easier to break.[146] In the case of a system dominated by Brownian noise, this means greater sensitivity to Brownian noise. With respect to the cantilever gap, a large gap results in more gas leakage and in the case of low pressure the beam behaves as an

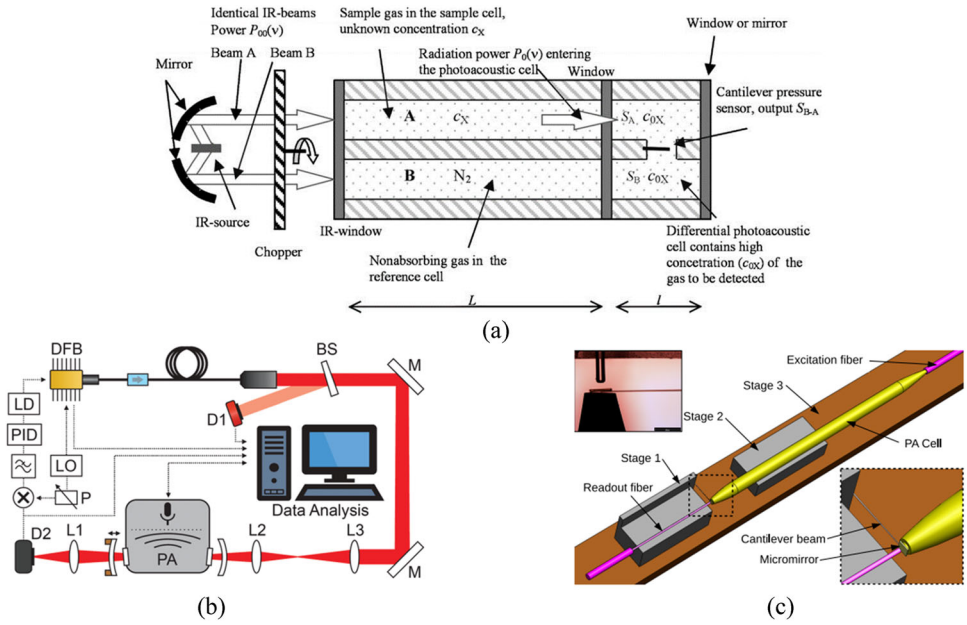

Figure 8. Different PAS reported in the literature. a) Differential PAS combined with direct absorption for better sensitivity and selectivity. Reproduced with permission.[178] Copyright 2005, Elsevier. b) Schematic view of CE-CEPAS. BS, M, PID, LD, and LO stands for beam splitter, mirror, lens, feed-back controller, laser driver, and local oscillator, respectively. Reproduced with permission.[184] Copyright 2019, Royal Society of Chemistry. c) Sketch of a PA system. (Insets) Enlarged sketch and microscopic views of the micro mirror alignment against the PA cell outlet and the readout fiber. Reproduced with permission.[149] Copyright 2017, The Optical Society.

undamped structure. The minimum gap that can be achieved is dependent on the minimum feature size of the lithography process[145] used in cantilever fabrication.

Cantilevers have been placed at different locations in the system. These include 1) the cantilever can be placed in the PA cell at one end of the cylinder while the excitation light comes from the other end as depicted in **Figure 8**c,[149] 2) both the excitation and readout fibers are on the same side,[177] and 3) the cantilever can be placed at the side of the cell.[128]

The detection of the cantilever's motion can be performed using a Michelson interferometer (MI),[178,179] Fabry–Perot cavity[180] or the piezoelectric effect.[175] The Fabry–Perot configuration can be a white-light based Fabry–Perot interferometer (WL-FPI),[180] in which the fiber end and the cantilever side constitute such a Fabry–Perot configuration, or a laser-based Fabry–Perot interferometer (L-FPI).[181] Fabry–Perot cavities are characterized by high sensitivity, small size and immunity to electromagnetic radiation.[139] Alternatively, Michelson interferometers can be used with a sensitivity down to a few picometers.[125] In the Michelson configuration, an iris can be placed in the path of the laser beam before impinging on the cantilever, which controls the size of the beam.[145] Its disadvantages are the higher cost and complexity.[159,182] In its simplest form, the cantilever deflection can be measured using a laser impinging on the cantilever with a certain incidence angle and the reflected light is detected using a quadrant detector.[142,152]

Cantilever-Enhanced PAS: Research describing the use of cantilevers in PAS is discussed in detail in the next sections. A summary of the detection limits reported in the literature can be found in Table 2. The details are given in the following subsections.

Optical-Based Detection: Kauppinen and co-workers (Gasera Ltd.) developed cantilever-enhanced photoacoustic spectroscopy (CEPAS) using a silicon-based cantilever[125] in which the vibration was detected using a Michelson interferometer. The modulation frequency was applied off the resonance of the cantilever. The group used such CEPAS to measure different gases including methane (CH_4),[178] carbon dioxide (CO_2),[144] hydrogen sulfide (H_2S),[183] and acetylene (C_2H_2).[184] The detection limits for these gases can be found in Table 2. Continuous development has lead to NNEAs around 10^{-10} $cm^{-1}W$ $Hz^{-0.5}$ using lasers. The sensitivity of the PA could be enhanced by combining the DAS and PAS,[178] as the absorption increases in the DAS when the path length is increased. The combined system is shown in Figure 8a. Two beams are directed to the absorption gas cells and finally the PA cell, where the cantilever measures the difference between the two acoustic signals due to the absorbed power of the two beams in the PA. The cell contains a known concentration c_{0X} of the gas to be measured. The differential signal will only be detected when the two beams are unbalanced by placing a gas of unknown concentration c_X in one of the two DA cells. This signal can be enhanced by increasing the absorption length, L. The PA cell provides the selectivity and dispenses with the need for a spectral filter or interferometer, unless there is a spectral correlation between the gas in the PA cell and another gas in the DA cell.[185] The detection limit of the measured methane, CH_4, was 10 ppb at a measurement time of 0.4 s using a black body source. Compact packaging of a differential PA cell with an MIR LED has been achieved with a side length of 40 mm.[186] A comparable detection limit was achieved using a spectral band pass filter instead of the differential configuration.[125]

Recently, Temmu et al.[184] applied the cavity enhancement techniques by placing the PA system inside a cavity, as shown in Figure 8b. The DFB laser has a wavelength of 1.53 μm and an output power of 7.5 mW. Lenses L2 and L3 are used to match the input beam to the cavity resonance. The cavity was formed using dielectric coated concave spherical mirrors. The cavity's length was 147 mm and the corresponding finesse was 200. Using such a configuration, the authors boosted the NNEA of the system by two orders of magnitude (1.75×10^{-12} $cm^{-1}W\ Hz^{-0.5}$). The corresponding detection limit of acetylene was 24 ppt using a 100 s integration time.

A simpler configuration, using a Fabry–Pérot (FP) system, shows performance in the same order of magnitude as a state of the art PAS using a Michelson interferometer (e.g., PAS by Gasera Ltd.). A micromirror, made of borosilicate coated with Cr and Au layers, with dimensions 300 μm × 300 μm × 30 μm (resonance frequency 914 Hz), was placed at one end of the cylinder while the excitation light was injected from the other end. The light was modulated at 457 Hz in order to detect the second harmonic signal of wavelength modulation at the resonance frequency of the cantilever. A detection limit of 15 ppb of acetylene (C_2H_2) was achieved with a measurement time of 0.3 s using a 23 mW C-band semiconductor laser with a wavelength of 1530 nm. The corresponding NNEA was 7.7×10^{-10} $cm^{-1}W\ Hz^{-1/2}$. The detection of the cantilever motion was performed using an FP system by placing a fiber tip in front of the micromirror instead of the Michelson-based detection used by Gasera.[149] The experiment was repeated with a Gasera PA device which showed a comparable NNEA of 2.5×10^{-10} $cm^{-1}W\ Hz^{-1/2}$. Zhou and Iannuzzi[177] installed the excitation and read-out fibers on the same side. They detected acetylene with an NNEA of 1.3×10^{-9} $cm^{-1}W\ Hz^{-1/2}$. The PA cell (nonresonant) was a tube of inner diameter 0.6 mm and length around 11 mm.

A comparison of the performance of a graphene-based cantilever and condenser microscope was reported by Zelinger et al.[187] The authors developed a multilayer graphene membrane and a multilayer graphene cantilever that were more sensitive than commercially available condenser microphones. Methanol was measured, and the detection limit was around 420 and 330 ppb for the membrane and cantilever, respectively as compared to 750 ppb for a commercial condenser microphone. The measurements were conducted using a CO_2 laser of 300 mW. The length of the cylindrical PA cell (nonresonant mode) was 107 mm with an inner diameter of 6 mm. The deflection of the beam was detected using a laser and a quadrant detector.[142] Suchánek et al.[188] measured acetone (C_3H_6O), acetic acid (CH_3COOH), and methanol (CH_3OH) using a circular cantilever made of mica. The corresponding detection limits of the gases were 24.8, 0.54, and 0.8 ppm at wavelengths 9.24, 10.24, and 9.5 μm, respectively. The laser power ranged from 170 mW to 1 W across these wavelengths.

Piezoelectric-Based Detection: Instead of using the optical detection methods for detecting the cantilever vibration, one could use a cantilever made from a piezoelectric material. In this case, the output piezoelectric signal, due to the film vibration, can be related to the PA signal. A polyvinylidene fluoride film used as a cantilever is such an example.[175] The film was placed on one side of the cylindrical PA cell whose length was 30 mm with an inner diameter of 5 mm. The PA cell was operated at its first resonant longitudinal mode (5296 Hz). The film's dimensions were 25 mm × 13.2 mm × 0.3 mm. Water vapor (H_2O) was detected with a detection limit of 40 ppm using a DFB laser at 1396 nm. The NNEA of the system was $2.4 \times 10^{-7}$$cm^{-1}W\ Hz^{-0.5}$,[175] which was even lower than that achieved using optical interferometry.

A PA sensor based on a silicon cantilever coated with a piezoelectric thin film of $Pb(Zr_x,\ Ti_{1-x})O_3$.[148] The detection limit was 1.6 mPa $Hz^{-0.5}$. Carbon dioxide (CO_2) gas was measured with a detection limit of 330 ppm at 4.25 μm. The IR source used was a micro-IR source followed by a selective IR filter at the absorption wavelength. The modulation frequency was 20 Hz. The PA cell was made of aluminum with an inner diameter of 8 mm and a length of 15 mm. The authors integrated the cell with the microphone and the micro-IR source on a printed circuit board.[129] Such a compact solution is required for applications involving high gas concentrations.

LED-Based PAS: A 455 nm LED with an average power of 90 mW has been used to excite the gas inside a PA cell in a nonresonant mode. The detection of the PA signal was conducted using a bare single mode fiber SM acting as a cantilever. The output light from the fiber was imaged on a displacement detector[143] as shown in **Figure 9**a. It is easy to control the fiber's resonance frequency by adjusting its length before use since the resonance frequency is inversely proportional to the square of the fiber length. The detection limit of NO_2 was 50 ppm. This technology has the advantage of simplicity and low cost but may not be suitable for mass production.

For detection in the MIR, MIR LEDs were used[144] to measure carbon dioxide (CO_2) with 11 ppm as a detection limit operating at 4.2 μm and a continuous power of 30 μW. Propane (C_3H_8) was also measured with a detection limit of 6 ppm using a LED at 3.4 μm and a continuous power of 150 μW with an integration time of 1 s. The PA cell was made of stainless steel with an inner diameter of 5 mm and a length of 42 mm. A cantilever (with dimensions of 10 mm × 3 mm × 10 μm) was placed in the middle of the cell. The cantilever resonance frequency was 1.07 kHz. The PA was modulated at 80 Hz, which was different from the resonance frequency of the cantilever.

For THz applications, a silicon cantilever has been developed for the PA detection.[145] The cantilever dimensions were 7 mm × 2 mm × 10 μm. The thickness of the cantilever gap was 3 μm and the resonance frequency was 280 Hz. The light was modulated at the resonance frequency of the cantilever. The PA cell was a cylinder made of stainless steel 50.8 mm long and 10 mm in diameter. The achieved NNEA was 4.28×10^{-10} $cm^{-1}W\ Hz^{-0.5}$ and the minimum detection limit of absorbance was $1.71 \times 10^{-5}cm^{-1}$ at 15 mTorr using a source power of 25 μ W at 400 GHz and an integration time of 0.5 s.[145,146] The beam deflection was detected using a Michelson interferometer with a reference mirror and the other mirror was the cantilever. The same group developed a compact cantilever based on a piezoelectric measurement system, where three thin films of a lead zirconate titanate (PZT) piezoelectric layer were sandwiched between two metal layers.[190]

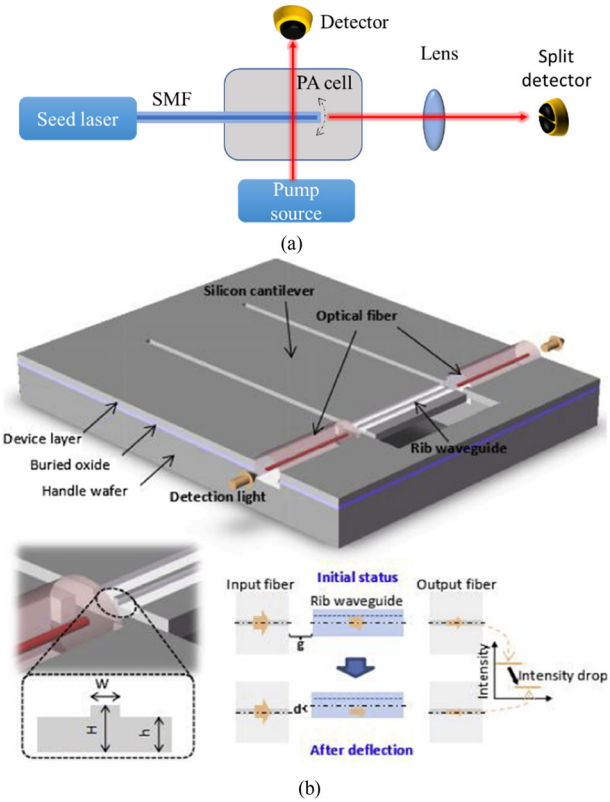

Figure 9. a) PA cell equipped with a single mode fiber (SMF) as a cantilever. The fiber was excited with a laser and the output light from the other side of the fiber was imaged on a displacement detector.[143] b) Cantilever with a rib waveguide on its top. By coupling light into the rib waveguide from one side and detecting the transmitted power from the other side, any deflection of the cantilever will affect the measured power, which is directly related to the deflection value. Reproduced with permission.[189] Copyright 2019, Elsevier.

Finally, a compact cantilever was described recently with dimensions 9.5 mm × 2.5 mm × 10 μm and a rib waveguide placed on its tip along the cantilever's width. The detection was conducted by measuring the fiber-to-fiber coupling with the rib waveguide placed in between, as depicted in Figure 9b. On applying an acoustic signal, the cantilever deflects, and the output intensity is changed due to the variation in coupling efficiency. The fibers were prealigned with an offset so that the ratio of the output power to the applied pressure was linear. The sensitivity was 8.3 V Pa^{-1} and the minimum detectable pressure was 35 nPa $Hz^{-0.5}$ at 150 Hz (the same resonance frequency as that of the cantilever).[189] Such a cantilever could be a good candidate for PAS.

Integration of Lasers, PA Cell, and Microphone: The research institute CEA LETI presented a platform for the full integration of a QCL, a differential Helmholtz PA cell, and an MEMS beam microphone. An array of QCLs emitting at different wavelengths covering the absorption wavelengths of the different gases used are depicted in **Figure 10**a. The outputs of the QCLs were multiplexed to a single waveguide using an arrayed waveguide multiplexer.[129] The microphone was fabricated by etching the beam on an SOI wafer on which a piezoresistive silicon nanogauge was attached to the beam, as depicted Figure 10b. With beam motion stress was induced on the nanogauge leading to a resistance change, which was measured using a Wheatstone bridge configuration.[191] Waveguides for light routing and the two chambers of the differential Helmholtz cell were fabricated on another wafer. The two capillary tubes connecting the two chambers of the differential Helmholtz cell were fabricated on a third wafer. Finally, all three wafers were stacked and bonded using eutectic bonding[129] as depicted in Figure 10c; this is considered a complicated and challenging process technology.[192]

2.3. Comparison between Photoacoustic and Direct Absorption in TLS

A comparison between the two systems using Equations (8) and (25) can be carried out based on the ratio between the minimum absorption coefficients in the PS system and the optical detector system. This ratio is given by

$$\gamma = \frac{\alpha_{\min \mathrm{PA}}}{\alpha_{\min \mathrm{DAS}}} = 9.6 \sqrt{\frac{R_i(\lambda)}{q\zeta P_o}} \left(\frac{\omega}{\omega_o}\right)^{1.25} \omega_o^{1.75}\, \theta_{\mathrm{PA}} l \Gamma_g \tag{28}$$

From the above equation, one can conclude the following. The DAS using lasers outperforms the PS system in the case of lower laser power and longer path length, $\left(\frac{\omega}{\omega_o}\right)^{1.25}\omega_o^{1.75}\theta_{\mathrm{PA}} l$. On the other hand, the PA system may be preferred when size is a limitation and there is a need for a compact gas cell since θ_{PA} is proportional to the cell area. The term $\left(\frac{\omega}{\omega_o}\right)^{1.25}\omega_o^{1.75}\theta_{\mathrm{PA}} l$ is dependent on the detector parameters in the DAS and on the PA cell in the PAS.

A general color plot of γ versus wavelength and source power is illustrated in **Figure 11**a for the unity value of the term $\left(\frac{\omega}{\omega_o}\right)^{1.25}\omega_o^{1.75}\theta_{\mathrm{PA}} l$. The white contour line represents the trajectory of the unity ratio. For longer wavelengths and lower power, the DAS outperforms the PAS.

For a given laser power, a PAS system (with a given modulation frequency, cell area, and cantilever thickness) can be compared to a DAS system (of a given path length l), to check which has a better sensitivity at the required wavelength of operation. For example, the high performance PA gas sensor[33,210] has the following parameters: (t_b = 10 µm, cell diameter equals to 4 mm) and the respective θ_{PA} equals 2.2 × 10^{-5} (Pa^{-1} kg $(mm)^3)^{-0.25}$. Then, in the case of ω/ω_o= 0.25 and f_o = 480, one can evaluate the term $\left(\frac{\omega}{\omega_o}\right)^{1.25}\omega_o^{1.75}\theta_{\mathrm{PA}}$ to be 5 $Hz^{1.75}$(Pa^{-1} kg $(mm)^3)^{-0.25}$. When compared to a laser-based DAS of path length 0.2 m, the term $\left(\frac{\omega}{\omega_o}\right)^{1.25}\omega_o^{1.75}\theta_{\mathrm{PA}} l$ will be unity. The corresponding plot is the same as Figure 11a.

With increasing path length (e.g., 20 m), the unity contour line will be moved to the upper left corner of the plot and the DAS will be the best performer for a larger range of laser powers and wavelengths. Therefore, for lasers with a power of a few mWs the DA systems with path lengths greater than tens of mms should provide better sensitivity. Increasing the power to hundreds of mWs or even greater, results in the PAS having better sensitivity as compared to the DAS with a path

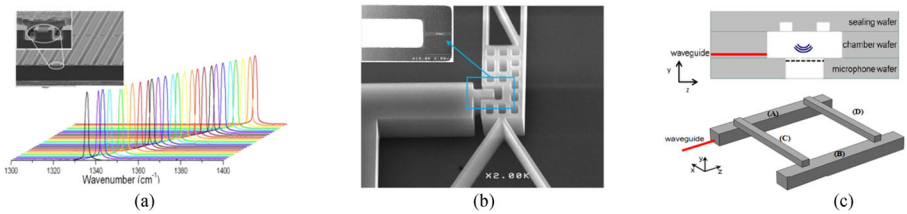

Figure 10. a) Emission wavelengths of an array of QCLs. The inset contains an SEM image of fabricated QCLs. b) SEM image of a microbeam with a nanogauge attached to the beam. c) Schematic view of a differential Helmholtz PA cell. (Top image: 3 stacked wafers for implementing the cell. The area in white represents hollow parts) (Lower image: 3D isometric view of the cell where the hollow part is in gray.) Reproduced with permission.[193] Copyright 2014, IEEE.

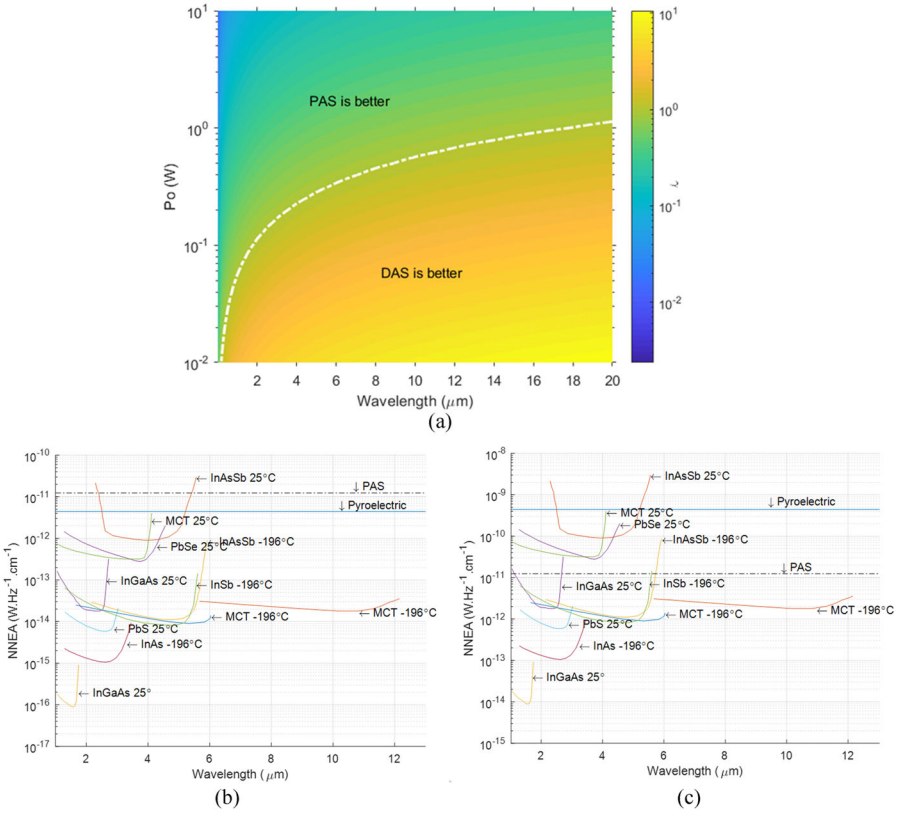

Figure 11. a) Color plot of the ratio of the normalized minimum absorption coefficient of the PA system to that of the DA system for different wavelengths and different laser powers in the case of unity system parameters $((\frac{\omega}{\omega_o})^{1.25}\omega_o^{1.75}\theta_{PA}l)$. The contour line represents the trajectory of unity ratio where for longer wavelengths and smaller powers, DAS is better. b,c) NNEA of DAS of different detectors (solid curves) (detector diameter = 1 mm), PAS (t_b = 10 μm, cell diameter = 5 mm, f_o = 500 Hz, $\frac{\omega}{\omega_o}$ = 0.25 (dashed dotted curves) where the path length = 1 m in (b) and the path length = 10 mm in (c).

length smaller than hundreds of mms. The same conclusion can be made when considering that high laser power saturates the optical detector which is not the case with PAS as it senses only the power absorbed by the gas not the transmitted power, making PAS favorable at high laser power levels. We want to emphasize that the above comparison is based on the theoretical fundamental limit, where the shot noise is the limiting factor of DAS. Thus, increasing the laser wavelength means increasing the number of photons and resulting in better sensitivity.

The NNEA for DAS in a shot noise limited system is inversely proportional to the square root of the input laser power as compared to the NNEA in the PAS, which is independent of the laser power. But as shown before, for a thermal noise limited DAS, the NNEA becomes independent of the laser power. Thus, one can plot the NNEA of the PAS together with the NNEA of the DAS (shown in Figure 5), to have a quantitative comparison between the two technologies. Compared to the PAS, the sensitivity of the DAS degrades at higher wavelengths due to the effects of thermal noise. For the PAS (dashed-dotted curve), the parameters were t_b = 10 μm, f_o = 500 Hz, $\frac{\omega}{\omega_o}$ = 0.25 and cell diameter = 5 mm. For the DAS, the diameter of the optical detector is 1 mm and path length is 1 m in Figure 11b and 10 mm in Figure 11c. To compare the PAS with the DAS with a path

length of 1 m or longer, the theoretical fundamental detection limit of DAS is better, except for the InAsSb detector operating at room temperature. Using detectors cooled down to −196 °C enhances dramatically the detection limit when compared to the PAS (i.e., NNEA = 10^{-14} W Hz^{-1} cm^{-1} using MCT cooled by nitrogen). However, if one is interested in applications involving small sampling volumes and short path lengths, the PAS is better than the DAS using thermal detectors or uncooled MCT or PbSe. However, InGaAs, PbS, and ultracooled detectors still have superior performance.

3. FTIR System

The FTIR spectrometers have a large spectral range which can simultaneously detect different gases. Good sensitivity can be achieved using the FTIR but it is less than the TDLS due to the use of a broadband light source instead of a powerful laser. The Michelson interferometer is the most common interferometer used in FTIR spectroscopy. The output light from the interferometer is modulated in the form of an interferogram versus time due to the interferometer's mirror motion. This interferogram is mathematically an autocorrelation function and consequently its Fourier transform gives the spectrum of the input light. In the FTIR-based DAS, a gas cell is placed between the light source and the interferometer. Thus, the spectrum measured by the spectrometer represents the gas transmission not the respective absorbance. The optical power is detected by an optical detector. In another configuration, the gas cell and interferometer positions can be swapped as was shown in Figure 1c. Replacing the gas cell and the optical detector with a PA cell and a cantilever leads to the FTIR-based PAS as depicted in Figure 1d. The modulated light output from the interferometer is coupled to the PA cell and the optical power, at the gas absorption wavelengths, is only absorbed by the gas. The absorbed light is further converted into an acoustic signal and is finally detected by the microphone (cantilever). The acoustic signal is in the form of an interferogram (i.e., autocorrelation function) but its Fourier transform corresponds to the spectrum of the absorbed power. Ideally, both systems should have the same absorption spectrum either, directly with the PAS or indirectly with the DAS. However, the detection method in the PAS depends on a heating mechanism (see Equation (12)), which may cause broadening of the absorption peaks leading to spectra that are different from those measured with direct absorption spectroscopy using an FTIR spectrometer.[214]

3.1. FTIR-Based DAS

The optical source used in the FTIR spectroscopy can be a filament source, a plasma source, a mode-locked laser,[215] light emitting diode LED[216] or a frequency-comb source. Usually, filament sources are used. They are made from silicon carbide (SiC) (Globar source) or ceramic rod (Nernst source) for the MIR range, whereas tungsten lamps are used for wavelengths lower than 5.5 μm (tungsten–halogen has a spectrum limited to 2.6). A plasma source can be used for wideband operation down to UV[217,218] with a larger radiance (equivalent T_{src} = 9000 K[217] or even more[219]) compared to filament-based sources at the expense of power consumption and source fluctuations. A frequency-comb source can also be used for wide band wavelength range measurements.[220]

Dual frequency comb spectroscopy is another approach to FTIR interferometry that does not require any moving parts.[221] It represents an emerging technology that combines the wide spectral range of FTIR with the high resolution and brightness of a laser. It is based on using two optical frequency combs (with slightly different repetition rates) where the light from one comb passes through the gas of interest. This is followed by an interference between the light from the two sources forming a beat signal, which is further detected by an optical detector. This is translated to a comb in the RF domain corresponding to the gas transmission spectrum.[221–223] This configuration has been used in open-path measurements of gases.[224,225]

The gas cell can be a multipass cell such as a White cell[2,22] or HWG.[226] The gas can also be placed inside a cavity and the corresponding technique is called incoherent broadband cavity-enhanced absorption spectroscopy. Compared to laser-based cavity enhanced spectroscopy, it is characterized by simplicity, the absence of any requirement for mode matching and mode-hop-free scanning, applicability to a spectral range starting from UV to infrared and simultaneous measurement of multispecies gases.[216,227–229] A detailed analysis on this technique is given by Platt et al.,[230] and a detailed review is provided by Zheng et al.[231] An open-air configuration can be used instead of a gas cell for measuring gases over long distances (open path FTIR).

The optical detectors used include InGaAs detectors which are often used when wavelengths of interest are less than 2.5 μm. InSb detectors that have a maximum detectivity for wavelengths less than 5.5 μm and MCT detectors that are used when the wavelength of interest ranges from 7.7 to 14 μm.[16,112]

Differential absorption spectroscopy is used to make quantitative measurements of gases regardless of the responses of the systems' components. Examples of these effects are the light source emission spectrum, the optical components' responses (e.g., mirror reflectivity in the cavity enhancement technique) and light scattering (e.g., open path measurements). In the case of using a gas cell, a background measurement could be performed (light passes through the gas cell devoid of the analyte of interest, e.g., contains only N_2 for IR spectroscopy) and the gas measurement is normalized to the background giving the gas transmission. In case of the cavity enhancement technique or open FTIR, a polynomial fitted to the gas measurement can be used to remove the background and the scattering effects.[222,232]

3.1.1. Theoretical Fundamental Detection Limit of FTIR-Based DAS

The average detector current, corresponding to the optical power coupled, is to some extent similar to Equation (7) and given by

$$i = \int_{\lambda_{min}}^{\lambda_c} B_{src}(\lambda')\,\zeta\,TP_o\,\eta\,R_i(\lambda')\,d\lambda' + \int_0^{\lambda_c} B_{BG}(\lambda')\,TP_d\,R_i(\lambda')\,d\lambda' \quad (29)$$

where the first term corresponds to the output optical power from the interferometer and the gas cell, TP_o is the spectrometer output throughput in Sr m^2 and TP_d is the detector throughput and is given by $\pi A_d \sin^2\theta_d$ (assuming Lambertian distribution of background emission), and λ_{min} is the minimum wavelength of operation of the system (limited by the beam splitter material or the detector). The maximum limit of the integration in Equation (29) is λ_c, which is the peak sensitivity of the detector (cutoff wavelength of semiconductor detectors), ζ represents the light transmission losses in the system, and B_{src} represents the spectral radiance of the black body source of temperature T_{src}.

The radiation pattern is assumed to be a Lambertian source (of constant radiance). The coupling reaches maximum when TP_d equals to TP_o. In such a case, using Equations (1), (3), and (29), the NEP is given by

$$\mathrm{NEP} = \frac{1}{R_i(\lambda)} \times \sqrt{2q\left(\int_{\lambda_{min}}^{\lambda_c} B_{src}(\lambda')\,\zeta\,TP_o\,R_i(\lambda')\,d\lambda' + \int_0^{\lambda_c} B_{BG}(\lambda')\,TP_o R_i(\lambda')\,d\lambda'\right)} \tag{30}$$

The second term under the square root can be neglected for the following conditions: small λ_{min}, compact spectrometer with low insertion losses (<10 dB) and $T_{src} > 500$ K (as the power $\propto T^4$ according to Stefan's law).

The linewidth of the gases is around a few GHz (tenths of cm^{-1} as mentioned before, while the reported resolution of the FTIR in gas sensing ranges from a few tenths up to tens of cm^{-1}, see the next section). Thus, the spectrometer resolution affects the measured absorbance. From the definition of the SNR in Equation (5), one should take into account the spectrometer resolution as follows

$$\mathrm{SNR}(\lambda) = \frac{P_o(\lambda)\,\zeta l\,\alpha(\nu) * \mathrm{sinc}\left(\nu\,\Delta\nu^{-1}\right)\Delta\nu^{-1}}{\mathrm{NEP}\sqrt{\Delta f}} \tag{31}$$

where $\Delta\nu$ is the spectrometer resolution in wavenumber, $\nu = 1/\lambda$ and $*$ denotes convolution. The sinc function represents the response function of the Fourier transform spectrometer (Fourier transform of a Boxcar function).[8] The mean output power P_o from the Michelson interferometer is expressed as the following (with the help of $\Delta\lambda = \lambda^2\Delta\nu$)

$$P_o(\lambda) = B_{src}(\lambda)\,\zeta\,TP_o\lambda^2\Delta\nu \tag{32}$$

It is assumed that the source spectrum is slowly varying with respect to the spectrometer resolution and gas absorption, thus it is excluded from the convolution (light source has a wide spectral range (black body)). The absorption coefficient $\alpha(\nu)$ is given by $\alpha(\nu) = \alpha_o f_g(\nu)$, where α_o is the absorption peak value and $f_g(\nu)$ is the gas line shape (normalized to one). The $f_g(\nu)$ has a Lorentzian profile ($\frac{\Delta\nu_g^2}{\Delta\nu_g^2+(\nu-\nu_o)^2}$) when the pressure is high as pressure broadening dominates, where $\Delta\nu_g$ represents the FWHM of the gas line shape and ν_o is its center. The $f_g(\nu)$ has a Gaussian profile ($e^{-\frac{(\nu-\nu_o)^2\ln 2}{\Delta\nu_g^2}}$) in case of high atmosphere (low pressure).[233] Using the Fourier transform properties, the absorbance peak ($\nu = \nu_o$), for a Lorentzian gas profile, is given by

$$A(\nu=\nu_o) = \alpha_o\,l\left(1-e^{-\frac{\Delta\nu_g\pi}{\Delta\nu}}\right)\log_{10}e \tag{33}$$

whereas for a Gaussian gas profile, the absorbance is given by

$$A(\nu=\nu_o) = \alpha_o\,l\,\mathrm{erf}\left(\frac{\pi\Delta\nu_g}{2\sqrt{\ln 2}\Delta\nu}\right)\log_{10}e \tag{34}$$

where erf corresponds to the error function. It is obvious that when $\Delta\nu \to \infty$, the absorbance peak reaches the extreme value $\alpha_o l\log_{10}e$. The normalized absorbance is depicted in **Figure 12**a. When $\Delta\nu \gg \Delta\nu_g$, the absorbance enhancement is linear with enhanced resolution ($\sim \frac{\Delta\nu_g\pi}{\Delta\nu}$ in the case of Lorentzian and $\frac{\Delta\nu_g}{\Delta\nu}\sqrt{\frac{\pi}{\ln 2}}$ in the case of Gaussian). Enhancement is saturated when resolution, $\Delta\nu$, reaches the gas linewidth $\Delta\nu_g$.

Thus, using Equations (6), (30), and (34), α_{min} at the absorbance peak is given by

$$\alpha_{min}(\lambda) \sim \frac{\theta_{DAS}}{R_i(\lambda)\,B_{src}(\lambda)\,\lambda^2}\sqrt{2q\int_{\lambda_{min}}^{\lambda_c} B_{src}(\lambda')\,R_i(\lambda')\,d\lambda'} \tag{35}$$

where θ_{DAS} is given by $(\sqrt{\zeta\,TP_o}\Delta\nu l\,(1-e^{-\frac{\Delta\nu_g\pi}{\Delta\nu}}))^{-1}$ or $(\sqrt{\zeta\,TP_o}\Delta\nu l\,\mathrm{erf}(\frac{\pi\Delta\nu_g}{2\sqrt{\ln 2}\Delta\nu}))^{-1}$, [cm $Sr^{-0.5}$] is the only parameter which depends on the parameters of the different system components and it is wavelength independent. The normalized α_{min} is plotted as a function of $\Delta\nu_g/\Delta\nu$ in Figure 12b. The α_{min} is saturated when $\Delta\nu \gg \Delta\nu_g$ (low resolution) because, within this region, increasing the resolution increases both the absorbance and the noise collected by the same factor. Improving the resolution further will not enhance the absorbance by the same factor and α_{min} degrades. Thus, it is better to operate at low resolution. However, this is not practical since it means that it is not possible to discriminate the absorption lines of different gases.

Increasing the interferometer throughput does enhance α_{min}, andincreasing the cell length also enhances the absorbance as long as no more losses are introduced, which can be taken into consideration in ζ. The mirror velocity does not affect the normalized absorption coefficient.

For a system having a minimum wavelength of detection, λ_{min} of 1 µm, one can color maps of the α_{min} for different absorption wavelengths and different T_{src}, for a unity θ_{sys} (e.g., $\zeta = 1$, TP = 0.01 (cm)^2 Sr, $\Delta\nu = 1$ cm^{-1} and $l = 100$ mm), as depicted in **Figure 13**a. The contour line of the minimum value of α_{min} for each value of T_{src} is plotted (solid line with markers), showing that the corresponding absorption wavelength increases as the source temperature decreases. An example of using an optical source of T_{src} of 2000 K, the minimum absorption coefficient at wavelength of 3 µm is 3×10^{-9} cm^{-1}, which corresponds to a detection limit of 0.1 ppb of methane (CH_4). For a system with a different θ_{sys}, one can directly multiply the plot by θ_{DAS}, where increasing θ_{DAS} means higher α_{min} (poorer detectivity).

Using a source with higher temperature enhances the detection limit only for short wavelengths (less than 8 µm for λ_{min} = 1 µm), whereas this is not the case for longer wavelengths due

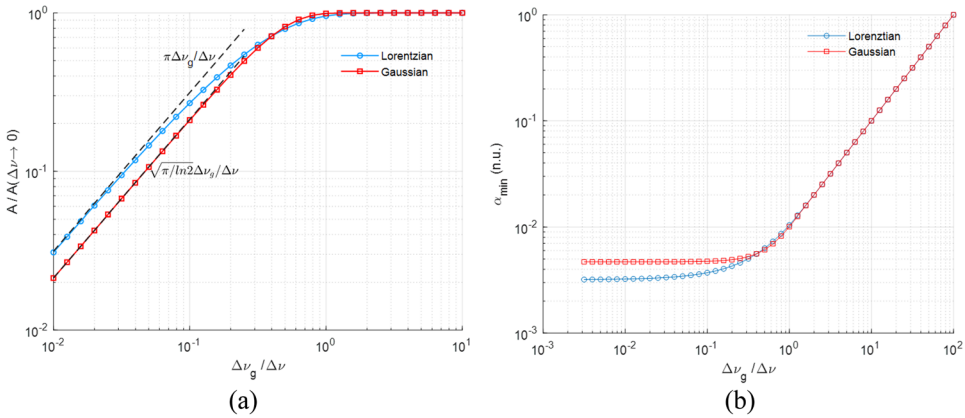

Figure 12. a) Normalized absorbance versus $\Delta\nu_g/\Delta\nu$ in the case of the Lorentzian and Gaussian profiles. Approximated linear lines for small $\Delta\nu_g/\Delta\nu$ are plotted in dashed black lines. b) Normalized α_{min} versus $\Delta\nu_g/\Delta\nu$ in the case of the Lorentzian and Gaussian profile.

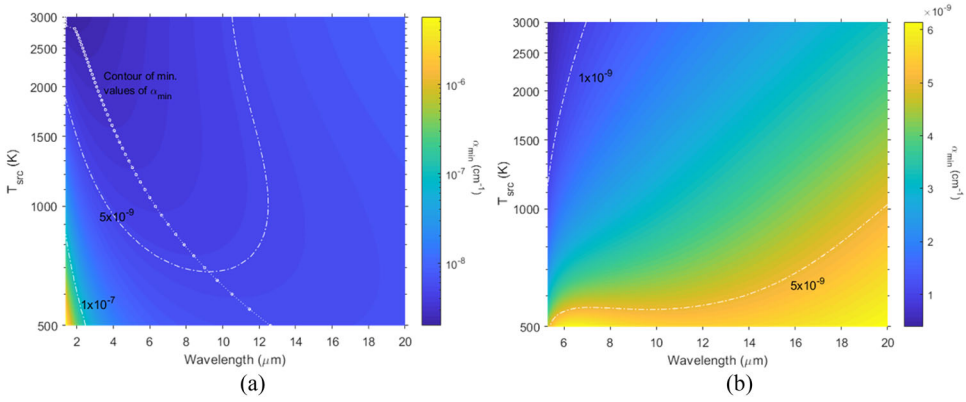

Figure 13. α_{min} versus wavelength and source temperature (θ_{sys} = 1) in case of a) λ_{min} = 1 μm, b) λ_{min} = 5 μm. Contour lines of different values of α_{min} are plotted. Also, the contour line of the minimum value of α_{min} is plotted if available.

to the increased shot noise (larger spectral power is absorbed). The situation is reversed in the case of increasing the minimum wavelength of detection (limiting the spectral range). That is why it is recommended that a filter is used to limit the spectral range of the spectrometer to only the spectral band of interest so as to decrease the shot noise.

3.1.2. Survey on FTIR-Based DAS Systems

Many researchers have reported on the use of multipass gas cells for measuring traces with detection limits down to ppt. The path lengths range from a few meters[7] to tens of meters[22,234] up to kilometers.[235] As an example, the detection limit of carbon dioxide (CO_2) was reported to range from 5 to 10 ppb[22] using a White cell of total path length L_T of 97.5 m and a resolution $\Delta\nu$ of 0.5 cm^{-1}. An analytical precision of 150 ppb of carbon dioxide (CO_2) using the FTIR spectrometer (Globar source, LN_2-cooled InSb, $\Delta\nu$: 1 cm^{-1}) and a White cell (L_T: 22 m) within a scan time of 8 min has been reported[234] and methane (CH_4) was measured with an analytical precision of 0.9 ppb under the same conditions. Methane (CH_4) was measured with an accuracy of 250 ppt using a White multipass cell (L_T: 24 m),[236] and nitrous oxide (N_2O) was measured with an accuracy of 50 ppt under the same conditions. For moisture measurements, a White cell (L_T: 10 m) and the FTIR spectrometer (LN_2-cooled MCT, $\Delta\nu$: 4 cm^{-1}) were used to achieve a lower detection limit of 15 ppb.[237] For measurements of tetrafluoromethane (CF_4) and hexafluoroethane (C_2F_6), the detection limit was 5 and 12 ppb, respectively, using a path length of 6.4 m.[7]

For very long path cells, a wide range of species, such as ammonia (NH_3), carbon monoxide (CO), formaldehyde (CH_2O), formic acid (HCOOH), methanol (CH_3OH,), nitric acid (HNO_3), nitric oxide (NO), nitrous oxide (N_2O), and ozone (O_3) were measured using a 1.26 km multipass cell (base path 23 m) with concentrations in the ppb range.[235] The deployment of an FTIR spectrometer (LN_2-cooled MCT, $\Delta\nu$: 0.5 cm^{-1}) on an aircraft for measuring atmospheric gases in conjunction with a White cell (L_T: 97.5 m).[22] The detection limits of methane (CH_4), carbon monoxide (CO), carbon dioxide (CO_2), nitrogen oxides (NO_x), and acetaldehyde (C_2H_4) ranged from 5 to 20 ppb.[22]

HWGs have been used as an alternative solution to multipass cells at the expense of sensitivity, due to the increased losses associated with the increased number of metal reflections (i.e., the

walls of the HWG). They are characterized by their small volume as compared to gas cells, which leads to shorter system response times making them useful for a real-time monitoring. A 1 m long hollow silica capillary waveguide with an inner coating of Ag/AgI has been used with the FTIR (SiC source, $\Delta\nu$: 4 cm^{-1}). With an averaging time of around 20 s, the lower detection limits for carbon dioxide (CO_2), methane (CH_4), and chloroethane (C_2H_5Cl) were calculated to be 15.8 ppb at 2358 cm^{-1} (4.24 μm), 512 ppb at 1304 cm^{-1} (7.67 μm), and 1.218 ppm at 982 cm^{-1} (10.18 μm), respectively.[226] Thompson et al. utilized an FTIR spectrometer followed by a hollow waveguide made of quartz inner coated with Ag/AgI, having a length of 0.55 m and an inner diameter of 2.1 mm to measure nitric oxide (NO) at around 2144 cm^{-1} (4.66 μm) and carbon monoxide (CO) at around 1875 cm^{-1} (5.33 μm). The output light was coupled to a liquid nitrogen-cooled MCT detector. The setup performance was compared to a multipass cell (3 m) instead of the HWG. The HWG response time was one-tenth that of the multipass cell and had ≈60% better sensitivity.[102]

FTIR spectrometers are widely used in open air with good detection limits. The typical detection limit of greenhouse gases can be down to few ppb.[3] An example of such an application is the measurement of volcanic gases in the open air using an FTIR spectrometer (LN_2-cooled MCT or InSb, $\Delta\nu$: 0.5 cm^{-1}).[238] A Nernst glower source was placed 135 m away from the spectrometer. The absorption sensitivity achieved was 10^{-4}. The corresponding sensitivity of methane (CH_4), carbon dioxide (CO_2), water (H_2O), hydrogen chloride (HCL), and sulfur dioxide (SO_2) were 419 ppb, 30 ppm, 710 ppm, 15 ppb, and 200 ppb, respectively.

Optical frequency comb-based supercontinuum sources have been used for gas analysis instead of filament-based sources. The emission lines of such sources have relatively high brightness. This leads to a higher signal to noise ratio or shorter measurement time[239] at the expense of cost. For example, an optical frequency comb source based on an optical parametric oscillator, with a wavenumber range from 2100 to 3600 cm^{-1}, was used to detect different gases with ppb detection limits.[240] The source was followed by a Herriot gas cell (L_T: 36.4 m) and a fast-scanning Michelson interferometer (thermoelectrically cooled MCZT detector, $\Delta\nu$: 0.014 cm^{-1}). The achievable detection limit was 0.5 ppb for carbon dioxide (CO_2) at 2350 cm^{-1} (4.25 μm) and 5 ppb for methane (CH_4) at 3020 cm^{-1} (3.3 μm) within 30 s. The normalized absorption coefficient was 3.8×10^{-8} $cm^{-1}Hz^{-0.5}$. Another frequency comb source used in conjunction with a multipass cell (L_T: 76 m) and FTIR spectrometer was able to measure methane (CH_4) at 3.3 μm and nitric oxide (NO) at 5.25 μm. The range of the minimum detectable concentrations was 10–20 ppb $Hz^{-0.5}$.[220]

Regarding miniaturized MEMS-based spectrometers, a Michelson-based FTIR spectrometer with a resolution 35 cm^{-1}, an InGaAs detector and a direct gas cell of length 100 mm.[10] The corresponding sensitivity of acetylene (C_2H_2) was 350 ppm using the absorption band at 6550 cm^{-1} (1.527 μm) and 1800 ppm for carbon dioxide (CO_2) using the absorption band at 4975 cm^{-1} (2 μm) and an averaging time of 8 s. Toluene (C_7H_8) was also measured with a detection limit of 90 ppb using a White gas cell (L_T = 20 m), with a resolution of 80 cm^{-1} and an average time of 1 min.[241]. Carbon dioxide (CO_2) gas was also measured in an open path of 6 m with an error of prediction of 1.8%.[242] Carbon dioxide (CO_2) and methane (CH_4) gases were measured using a lamellar grating MEMS FTIR spectrometer ($\Delta\nu$: 20 cm^{-1} and measurement time 5 s) with a minimum measurable concentration of 10 and 100 ppm for the corresponding absorption bands at 4.25 and 3.3 μm, respectively. The light source was a halogen lamp, and a White cell of a path length 6 m was used.[243]

A summary of the detection limits reported in literature can be found in **Table 3**. From the above survey and from Equation (35), one can conclude the following. To reduce the detector thermal noise and reach maximum performance (shot noise limit), liquid nitrogen cooling is used especially for detectors in the MIR. The minimum absorption coefficient of the MEMS-based spectrometers is worse than that of benchtop spectrometers due to their small throughput. This is clear in the detection limits of different gases such as carbon dioxide (CO_2) and methane (CH_4) which are within the ppm range as compared to the ppb or ppt range of benchtop spectrometers. Using a frequency comb as the light source, at the expense of cost, means there is a wide band source of radiance B_{src} greater than that of the thermal sources due to the high laser power used. This is translated into better sensitivity, which is clear in the detection limits achieved for carbon dioxide (CO_2) and methane (CH_4). This is comparable or even better than that achieved with the thermal sources although the resolution was 0.014 cm^{-1} in case of an optical comb as compared to a few cm^{-1} with the other source (sensitivity is inversely proportional to resolution). A reasonable resolution for gas sensing using FTIR is a few cm^{-1}. It is also important to note that the detection limit is enhanced as a function of the square root of the optical power, due to the increased shot noise.

3.2. FTIR-Based Photoacoustic Spectroscopy

In the FTIR-based PAS, the spectrometer can be operated in one of two modes: rapid scanning or step scanning. The rapid mode is the conventional mode of operation, where the mirror of the Michelson interferometer is in continuous motion with a given velocity v_M. Such motion leads to a wavelength-dependent modulation (sinusoidal interferogram of each wavelength with a frequency related to its respective wavelength). The respective frequency is given by $f = 2v_M/\lambda$,[247] which is the same frequency as the PA signal. This results in a high frequency of operation. In the case of step scanning, the mirror is moved in step scan mode, which requires an additional optical modulator after the interferometer to modulate the light for the PA cell. The next analysis will focus on the continuous scanning mode.

3.2.1. Theoretical Fundamental Detection Limit of FTIR-Based PAS

As was seen in Figure 1d, and according to the prior analyses, having as small a PA cell area as possible is better, given that all the interferometer output power is coupled to the PA cell. Thus, the optimum cell area A_{cell} is given when the cell throughput $\pi A_{cell} \sin\theta_{cell}^2$ equals the interferometer throughput. For a PA cell

Table 3. Summary of FTIR-based DAS systems. λ_o is the wavelength/band of detection, SLED stands for superluminescent light emitting diode, LN_2 stands for liquid nitrogen, and Src. is the source.

Instrument (Src./detector)	$\Delta\nu$[cm^{-1}]	λ_o[μm]	Gas cell Type	Path length [m]	Gas	Detection limit/ scan time [s]	Ref.
Globar Src./LN_2-cooled InSb	1	3.3	White MP	22	CH_4	0.9 ppb/480	[234]
			White MP	24	CH_4	0.25 ppb	[236]
SiC Src.	5	7.67	HWG	1	CH_4	512 ppb/20	[192]
LN_2-cooled MCT or InSb	0.5	3.3	Open path	135	CH_4	419 ppb	[198]
Frequency comb Src./cooled MCZT		3.3	Herriot MP	36.4	CH_4	5 ppb	[200]
Frequency comb Src./cooled MCZT		3.3	MP	76	CH_4	10–20 ppb Hz^{-1}	[220]
MEMS FTIR/halogen source	20	3.3	White MP	6	CH_4	100 ppm/5	[243]
LN_2-cooled MCT	0.5		White MP	97.5	CH_4	5–20 ppb	[22]
LN_2-cooled MCT or InSb	0.5	4.186	Open path	135	CO_2	30 ppm	[198]
Frequency comb Src./cooled MCZT		4.25	Herriot	36.4	CO_2	0.5 ppb	[200]
	0.5		White MP	97.5	CO_2	20 ppb	[22]
Globar Src./LN_2-cooled InSb	1	4.4	White MP	22	CO_2	150 ppb/480	[234]
SiC Src.	4	4.24	HWG	1	CO_2	15.8 ppb/20	[192]
MEMS FTIR/halogen Src.	20	4.25	White MP	6	CO_2	10 ppm/5	[203]
MEMS FTIR/InGaAs	–	2	Direct gas cell	0.1	CO_2	1800 ppm/8	[10]
LN_2-cooled MCT	4	–	White MP	10	H_2O	15 ppb	[237]
–	–	–	–	6.4	CF_4	5 ppb	[7]
MCT	0.5		Gas cell	5	CF_4	≈ ppb	[244]
–	–	–	–	6.4	C_2F_6	12 ppb	[7]
MCT	0.5	–	Gas cell	5	C_2F_6	≈ ppb	[244]
LN_2-cooled MCT	0.5	–	White MP	97.5	C_2H_4	5–20 ppb	[22]
LN_2-cooled MCT	0.5	–	White MP	97.5	CO	5–20 ppb	[22]
Globar Src./LN_2−cooled InSb	1	4.7	White MP	22	CO	0.3 ppb/480	[234]
SiC Src.	6	10.18	HWG	1	C_2H_5Cl	1218 ppb/20	[192]
LN_2-cooled MCT or InSb	0.5	3.775	Open path	135	H_2O	710 ppm	[198]
LN_2-cooled MCT or InSb	0.5	3.517	Open path	135	HCL	15 ppb	[198]
LN_2-cooled MCT or InSb	0.5	3.992	Open path	135	SO_2	200 ppb	[198]
(MEMS FTIR) InGaAs	35	1.527	Direct gas cell	0.1	C_2H_2	350 ppm/8	[10]
(MEMS FTIR) PbSe	80	3.3	White MP	20	C_7H_8	90 ppb/60	[241]
Frequency comb Src./cooled MCZT		5.25	MP	76	NO	10–20 ppb Hz^{-1}	[220]
/MCT	0.125	5.41	White MP	16	NO	<20 ppb	[245]
		6.31			NO_2	<50 ppb	
		4.53			N_2O	<5 ppb	
–			White MP	24	N_2O	0.05 ppb	[236]
Globar Src./LN_2-cooled InSb	1	4.5	White MP	22	N_2O	0.3 ppb/480	[234]
/DLaTGS	0.5	0.662	MP	204	NO_3	6 ppt	[246]
	0.5		MP	204	C_3H_6O	10 ppb	
SLED	16	1.6	Cavity	1250	C_4H_6	600 ppb/240	[216]

with a maximum acceptance angle ($\theta_{cell} = \pi/2$), P_o is rewritten as

$$P_o(\lambda) = B_{src}(\lambda)\,\zeta\pi A_{cell}\lambda^2\Delta\nu \tag{36}$$

whereas Equation (6) will be as follows

$$\mathrm{SNR} = \frac{P_o C\,\alpha(\nu) * \mathrm{sinc}\left(\nu\,\Delta\nu^{-1}\right)\Delta\nu^{-1}}{\Delta x_n\sqrt{\Delta f}} \tag{37}$$

Using Equations (25), (36), and (37), α_{min} for the Lorentzian peak is given by

$$\alpha_{min} = \frac{4\omega}{(\kappa-1)\,\pi B_{src}(\lambda)\,\zeta\;\lambda^2\Delta\nu\left(1-e^{-\frac{\Delta\nu_g\pi}{\Delta\nu}}\right)} \times\sqrt{\frac{3K_B T_{BG}\;\pi\omega_o}{\lambda_n^2 t_b}}\sqrt{\frac{3\rho_g\rho_b\omega\mu}{2E}} \tag{38}$$

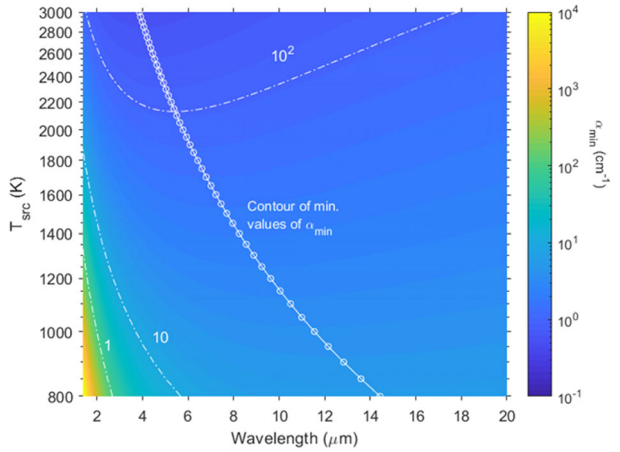

Figure 14. α_{min} of the FTIR-based PAS as a function of wavelength and source temperature ($\theta_{sys_{PA}} = 1$).

λ_o is the corresponding wavelength at the resonance frequency ω_o and the maximum frequency of operation $\omega_{max} = 0.25\omega_o$, for operation out of the resonant mode of the cantilever. This means that the minimum wavelength of operation of the interferometer can be related to λ_o by $\lambda_{min} = 4\lambda_o$. Then, α_{min} will be

$$\alpha_{min} \approx 726 \frac{\theta_{PA}}{B_{src}(\lambda)\ \lambda^{3.25}(\kappa - 1)} \sqrt{\frac{K_B T_{BG} \sqrt{\rho_g \mu}}{\lambda_{min}}} \tag{39}$$

where θ_{PA} is wavelength independent, depends on the parameters of different components and is given by

$$\theta_{PA} = \frac{1}{\zeta\ \Delta\nu \left(1 - e^{-\frac{\Delta\nu_g \pi}{\Delta\nu}}\right)} \sqrt{\frac{\nu_M^{3.5}}{\lambda_n^2 t_b}} \sqrt{\frac{\rho_b}{E}} \tag{40}$$

α_{min} has the same dependence on resolution as in the FTIR-based DAS. It is important to note that the acoustical noise is assumed to be small with tight PA cell seals. To illustrate the dependence of the system on wavelength, α_{min} is plotted for different source temperatures T_{src}, at unity θ_{PA} and $\lambda_{min} = 1$ µm, in **Figure 14**. For systems with different θ_{PA}, one just multiplies the plot by $\theta_{sys_{PA}}$. From these curves, it is clear that for longer wavelengths, the detection limit is better. This is because the longer wavelengths correspond to lower frequencies of modulation (PA signal $\propto \omega^{-1}$, due to heat conduction response time). One can also observe the following: 1) increasing the resonance frequency (decreasing λ_{min} (down to UV)) degrades α_{min}, 2) increasing the source radiance (higher optical source temperature) and decreasing the background temperature enhances the detection limit, 3) the detection limit is enhanced linearly with the source brightness, which is an advantage compared to the DAS, and 4) the detection limit is directly proportional to $\nu_M^{1.75}$. Thus, the mirror velocity should be operated in step mode or with slow motion (less than 0.1 m s^{-1}) to avoid such notable degradation in performance.

3.2.2. Survey on FTIR-Based PAS Systems

Step Scan: An example of a step scan FTIR-based PAS is depicted in **Figure 15**b. The output of a step scan Michelson interferometer was modulated using a chopper and the modulated light was injected into T-shaped PA cells.[248] The T-shaped cell consisted of three cylinders: an absorption cylinder, a resonant cylinder and a buffer cylinder as depicted in Figure 15a. The absorption cylinder was connected perpendicularly through the buffer with the resonant cylinder (resonance frequency is 342 Hz).[249] The T-cell was equipped with a condenser microphone (sensitivity 25.1 mW Pa^{-1} at 1 kHz). Using a Globar source emitting 12.6 µ W around 4.3 µm, the detection limit of carbon dioxide (CO_2) was expected to be 4 ppm. The cell works under ambient conditions, which is an advantage in using step scan FTIR spectrometers. The same design was reconfigured for differential measurement of acetylene and carbon dioxide (CO_2) in the presence of significant interference from ambient water vapor.[250]

Rapid Scan:

Microphone-Based PAS: Using a commercial FTIR spectrometer (Perkin Elmer, $\Delta\nu$ = 8 cm^{-1}, velocity : 0.5 mm s^{-1}) equipped with a dual microphone and a PA cell, the lower detection limit was determined to be 2 ppm for carbon tetrachloride (CCl_4) at 795 cm^{-1} and 5 ppm for trichloroethylene at 942 cm^{-1}.[251] The average time was greater than 100 s. Using another commercial FTIR spectrometer (Bruker IFS 131) equipped with a PA cell 20 mm long and a microphone, the absorbed light spectrum from 500 to 3000 cm^{-1} of methyl alcohol was compared with an infrared detector.[252] A different commercial FTIR gas analyzer ($\Delta\nu$: ranges from 10 to 15 cm^{-1}) based on photoacoustic detection was used.[253] The detection limit was 0.2 ppm for ethyl acetate and 2.5 ppm for benzene (C_6H_6), toluene ($C_7(H_8)$, and xylene ($(CH_3)_2C_6H_4$) at atmospheric pressure. The measurement time was 52 s.[253]

Cantilever-Based PAS: A 100 mm long PA cell equipped with a cantilever, with dimensions 4 mm × 1.5 mm × 10 µm and a gap of 3–5 µm, was used in conjunction with a commercial FTIR spectrometer (Mattson Galaxy 6020 series; the velocity was 0.9 mm s^{-1} OPD and the resolution was 8 cm^{-1}) to detect CH_4 at atmospheric pressure. The detection limit was 3 ppm with a measurement time of 168 s.[254] Methane (CH_4) was also measured using the same interferometer and a DTGS detector (FTIR-DAS).[254] The sensitivity of the PAS system corresponds to the FTIR based on the DTGS with an equivalent length of 60 mm. For enhanced performance, the same group used another cantilever with dimensions of 6 mm × 1.5 mm × 10 µm, and a gap distance of 5 µm. The PA cell was 100 mm long (a mirror was used at the end of the cell to double the absorption path) and the inner diameter was 4.5 mm. The PA system was used with another commercial FTIR spectrometer (Bruker Matrix series). The resolution was adjusted to 4 cm^{-1} and the velocity was around 1 mm s^{-1}OPD. Light injected into the PA cell had a spot size of 4.4 mm and divergence angle equal to 0.163 rad. The detection limit for methane (CH_4) (1 σ) was 0.5 ppm at 3017 cm^{-1} and 4 ppm for CO_2 at 3250 cm^{-1} with a 100 s measurement time. The pressure was 47 kPa.[255] The lower performance of the FTIR spectrometer, as compared to the

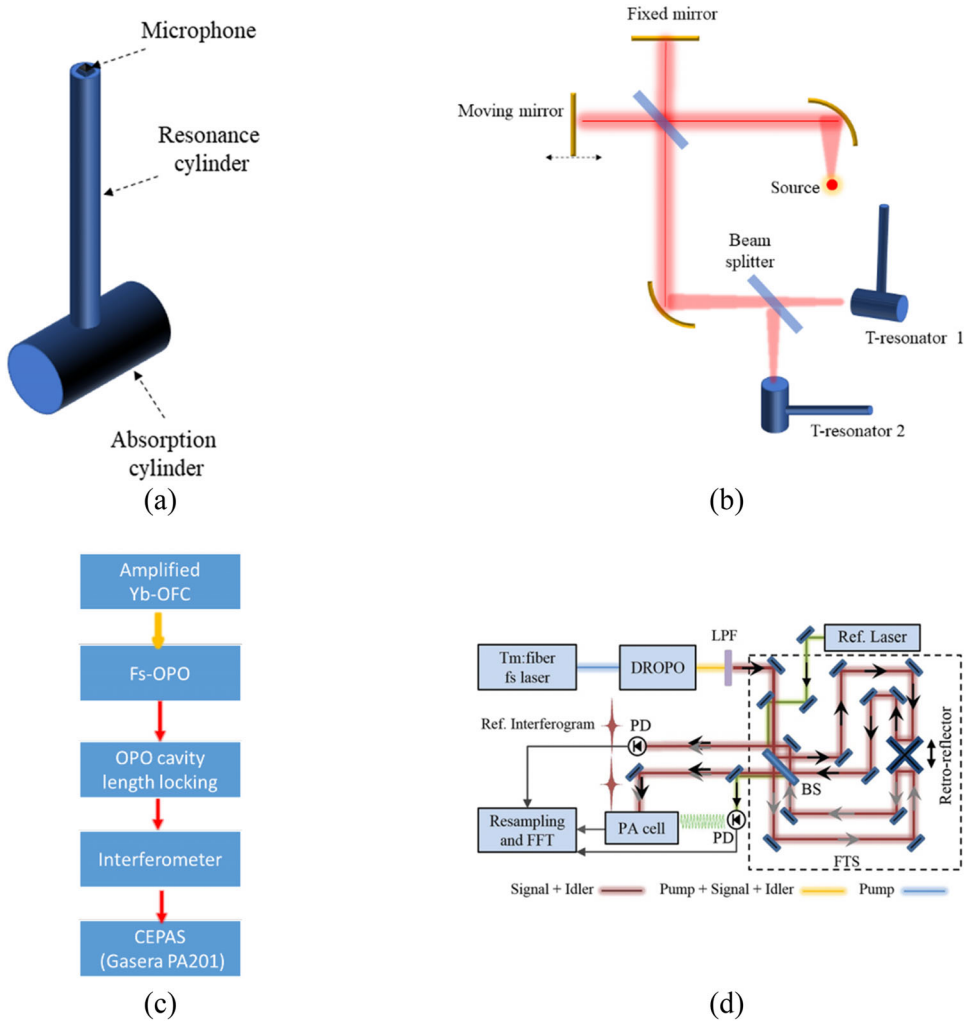

Figure 15. a) PA T-cell. b) Schematic of gas measurement using the FTIR spectrometer and the T-cell.[256] c) Schematic picture using the OPO oscillator (amplified ytterbium frequency comb) with the FTIR and PA cell to detect a methane isotope.[28] d) FTIR-based PA spectrometer using optical frequency comb. DROPO, LPF, BS, FTS, and PD holds for doubly resonant optical parametric oscillator, long pass filter, beam splitter, Fourier transform spectrometer and photodiode, respectively. Reproduced with permission.[171] Copyright 2018, Royal Society of Chemistry.

laser source or blackbody source followed by filters, is attributed to the limited throughput of the spectrometer (small divergence angle). In general, this group used a Michelson interferometer to detect the cantilever motion, where the variation in laser fringes is detected using four quadrant photodiodes. The cantilever was operated out of resonance (resonance frequency ≈ 480 Hz).

The OPO oscillator has been used as a light source with a commercial FTIR spectrometer (FS120, Bruker) and a DTGS detector (PVI-2TE-5, VIGO). The spectrum of the light source was measured using this configuration. The DTGS detector was followed by a commercial CEPAS (PA201, Gasera) and the methane isotope ($^{14}CH_4$) was measured at a pressure of 25 kPa and a temperature of 25 °C, as depicted in Figure 15c. The scanning speed of the mirror of the interferometer was adjusted to 1.4 mm s^{-1} to be compatible to the limited bandwidth of the CEPAS. The PA spectrum was normalized to the spectrum taken by the DTGS detector to eliminate the source power from the spectrum. The detection limit was less than 100 ppb.[28]

The supercontinuum source can be used to enhance the sensitivity of the FTIR-based PAS.[257] In this study the output light was coupled to the FTIR spectrometer (Bruker IR cube, $\Delta\nu = 4$ cm^{-1}, mirror velocity: 1.6 kHz) followed by the PA cell. The cell length was 100 mm, and the diameter was 4.5 mm. The pressure was at 1 bar and the temperature was 50 °C. The cantilever dimensions were 6 mm × 1.5 mm × 10 µm. The absorption of water $H_2(O)$ and methane (CH_4) were measured at 1.9 and 3.3 µm, respectively. The supercontinuum laser average power was 414 mW whereas the power spectral density at 1.9 µm was 275 µ W nm^{-1}. The measurements were compared to those using a black body source. The power enhancements were 70 and 19 times at 1.9 and 3.3 µm, respectively. However, the enhancements in the SNR were 13 and 1.6 at 1.9 and 3.3 µm, respectively. This was due to the increased pulse fluctuations of the supercontinuum source. For a 50 s averaging time, the detection limits of methane (CH_4) were 2.6 and 1.4 ppm for the black body and supercontinuum sources, respectively.

Table 4. Summary of work on FTIR-based PAS systems.

Excitation source	Velocity (OPD) [mm s^{-1}]	Cantilever dimensions (L [mm] × W [mm] × t [μm])	Cell dimensions (radius [mm] /length [mm])	Pressure [Torr]	Gas	Detection limit/ average time [s]	Ref.
Thermal	0.9	4 × 1.5 × 10	/100	–	CH_4	3 ppm/168	[211]
Thermal	1	6 × 1.5 × 10	2.25/100	353	CH_4	0.5 ppm/100	[212]
Thermal	1	6 × 1.5 × 10	2.25/100	353	CO_2	4 ppm/100	[212]
OPO oscillator	1.4	6 × 1.5 × 10	–	188	$^{14}CH_4$	100 ppb	[28]
OPO oscillator	–	–	–	150	$^{14}CH_4$	3 ppb	[258]
Supercontinuum	–	6 × 1.5 × 10	2.25/100	760	CH_4	1.4 ppm	[238]
Supercontinuum	–	–	2/97	–	CH_4	32 ppb/40	[259]
Frequency comb	1.6	6 × 1.5 × 10	2.25/100	760	CH_4	0.8 ppm/200	[160]

An optical frequency comb source was also used with the FTIR spectrometer and PA gas cell, as depicted in Figure 15d.[171] The optical frequency comb consisted of a pump laser followed by a doubly resonant OPO and filter. The emission signals were the signal comb (3.1–3.6 μm) and idler comb (4.6–5.4 μm). The spectrometer was custom made in which the two mirrors of the two paths of the Michelson interferometer were the two sides of the retroreflector mirror to double the resolution for same travel range. The mirror velocity was 1.6 mm s^{-1} and the resolution was 0.0037 cm^{-1}. One of the two outputs of the FTIR spectrometer was coupled to a photodetector for signal normalization and the other was coupled to a commercial PA gas cell (PA201, Gasera). The lower detection limit of methane (CH_4) was 0.8 ppm at 3.3 μm for an average time of 200 s. The pressure was 1 bar, and the power spectral density was 42 μW cm^{-1}. A summary of research in this field can be found in **Table 4**.

3.3. Comparison between Photoacoustic and Direct Absorption in FTIR Spectroscopy

A comparison between the two systems based on FTIR spectroscopy, using Equations (35) and (39), can be expressed by the ratio of the minimum absorption coefficient in the PAS system to that of the DAS. This is given by

$$\gamma = \frac{\alpha_{\min \mathrm{PA}}}{\alpha_{\min \mathrm{DAS}}} = \Omega_{\mathrm{g}} \frac{\theta_{\mathrm{PA}}}{\theta_{\mathrm{DAS}}} \frac{R_i(\lambda)}{\lambda^{1.25}\sqrt{\int_{\lambda_{\min}}^{\lambda} B_{\mathrm{src}}(\lambda') R_i(\lambda') \mathrm{d}\lambda'}} \tag{41}$$

where $\alpha_{\min \mathrm{PA}}$ and $\alpha_{\min \mathrm{DAS}}$ represent the normalized minimum absorption coefficient for the FTIR-based PAS and the FTIR-based DAS, respectively. The parameter Ω_{g} is given by

$$\Omega_{\mathrm{g}} = 513\sqrt{\frac{K_{\mathrm{B}} T_{\mathrm{BG}} \sqrt{\rho_{\mathrm{g}} \mu}}{q \lambda_{\min} (\kappa - 1)^2}} \tag{42}$$

From the above equation, the following conclusions can be drawn: 1) regarding the interferometer parameters, the ratio between the two systems is independent of the resolution as both have the same dependence on the resolution, 2) on the other hand, the shorter measurement time (i.e., higher mirror velocity v_{M}), the better the DAS is compared to the PAS ($\theta_{\mathrm{PA}} \propto v_{\mathrm{M}}^{1.75}$). This is clear in the literature survey where PAS-based FTIR spectrometers have lower mirror speeds (less than 1 mm s^{-1}). 3) The DAS is better for higher interferometer throughput (TP_o) given that the output light fills all the detectors (PA cell in PAS or optical detector in DAS). This can be stated in another way. A PAS with a smaller cell area is preferable (cell diameter is usually a few mms or even tenths of mms), thus there is no need for an interferometer with a large throughput, whereas in the DAS-based FTIR spectrometer, in the case of a shot noise limited detector, having a larger throughput and detector area means more signal ($\theta_{\mathrm{DAS}} \propto \mathrm{TP}_{\mathrm{o}}^{-0.5}$). 4) For the optical source, increasing its temperature enhances the performance of the photoacoustic-based system compared to the optical one, due to the increased shot noise in the latter. This is clear in **Figure 16**a,b. In addition, this also applies to increasing the wavelength for a given $\lambda_{\min}$ and for increasing $\lambda_{\min}$ (lower f_o), given that the seal effectively blocks acoustical noise. 5) Increasing the cell length, l, enhances the performance of the DAS over the PAS provided that the introduced losses, due to the mirrors, does not mask such enhancement. In general, the cell length and the mirror velocity are the dominating factors in specifying which is better.

4. Conclusion and Outlook

A critical review has been conducted on gas sensing using DAS and PAS. Each method was analyzed when using either a tunable laser source or a Fourier transform spectrometer. In the case of PAS, the survey and the analyses were focused on the cantilever due to its high performance. The review includes analyses of the different cantilevers described in the literature that vary in size, material composition, and vibration detection methods. The recent techniques developed to enhance gas detection limits including different excitation sources, system architectures, and detectors are discussed. The achieved detection limits of different gases are summarized in addition to the corresponding system parameters.

A theoretical analysis was conducted on these systems to find the fundamental detection limits for each system. To compare the DAS and the cantilever-based PAS, a figure of merit was used which was defined as the ratio between the normalized absorption coefficients (normalized with respect to measurement time) of each system. The NNEA coefficient was also used to compare the systems when using a tunable laser. The derived

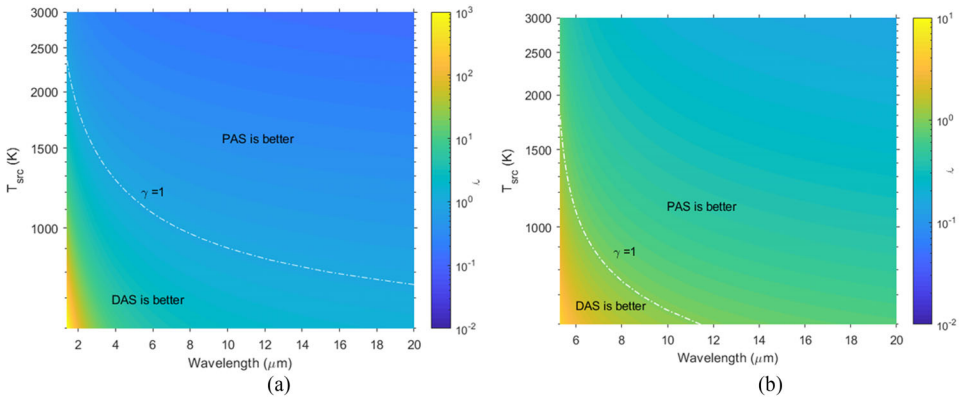

Figure 16. a,b) Ratio of the absorption coefficient of the FTIR-based PAS and FTIR-based DAS as a function of wavelength for different light sources and unity ratio of $\frac{\theta_{PA}}{\theta_{DAS}} = 10^{-9}$ The contour line represents the trajectory of unity ratio where for longer wavelengths and higher source temperature, PAS is better: (a) $\lambda_{min} = 1$ μm, (b) $\lambda_{min} = 5$ μm.

relations are a function of the characteristics of the systems including their source power, wavelength of operation, system throughput, and detector parameters such as detector size and cooling temperature. The relations allow the user to choose between the DAS and PAS given other system parameters. When using a tunable laser, direct absorption spectroscopy is better for lower laser power levels and longer gas cells and the converse is also true. For the FTIR-based systems, a direct absorption spectroscopy system is better than a PA-based system for lower source temperatures, higher spectrometer throughputs (bench-top spectrometer), faster mirror velocities, and longer gas cells.

Gas sensors, based either on lasers or Fourier transform spectrometers, are high performance sensors in terms of selectivity, sensitivity, and wideband range. Their application scope is expected to increase due to the increasing demand for air pollution monitoring. Such trends will contribute to reducing the impact of pollution on health and on climate change and the related increased government regulations for industries. The growth of the internet of things, smart cities, and health care requires large-scale deployment of cheap and highly sensitive sensors to enable detection of VOCs at ppb levels. This involves wearable gas sensors, sensors integrated into smartphones, in cars, buildings and houses. Such progress would facilitate high-resolution pollution mapping in cities on a large scale. To this end, the biggest challenge is the mass production and at low-cost of miniaturized multiple-gas sensors with sufficient selectivity and sensitivity. Photoacoustic technology represents a good candidate for small gas cells with expected additional improvements in the silicon integration of photoacoustic cells and microphones. On the other hand, laser miniaturization and integration will continue, given the large investments in the silicon photonics industry. Once robust integration is achieved, cascading of laser sources of different wavelengths on the same chip will facilitate multi-gas measurement. A recent advancement of optical comb light sources, making use of the nonlinearity of the silicon/silicon nitride-based cavity, enables the generation of wide band spectrum from a single laser source, which can be further integrated on same chip.[260,261] Such a source can be used either in conjunction with an FTIR or in dual frequency comb mode with the need for small RF spectrum analyzers. More development is needed in this direction for example to enhance the flatness of the spectrum. MEMS FTIR spectrometers are considered a good solution with a resolution limited to 10 cm^{-1}, but are physically limited by actuator travel range, and a moderate sensitivity, which is determined by the MEMS throughput/size. Even though they are very small and reasonably cheap, they are not yet compatible with all gas sensing applications.

Conflict of Interest

The authors declare no conflict of interest.

Keywords

detection limits, FTIR, gas sensing, NNEA, normalized absorption coefficient, photoacoustics, tunable lasers

Received: September 28, 2021
Revised: March 12, 2022
Published online: May 10, 2022

[1] X. Liu, S. Cheng, H. Liu, S. Hu, D. Zhang, H. Ning, *Sensors* **2012**, *12*, 9635.
[2] D. W. T. Griffith, N. M. Deutscher, C. G. R. Caldow, G. Kettlewell, M. Riggenbach, S. Hammer, *Atmos. Meas. Tech. Discuss.* **2012**, *5*, 3717.
[3] L. Shao, P. R. Griffiths, A. B. Leytem, *Anal. Chem.* **2010**, *82*, 8027.
[4] J. B. McManus, J. H. Shorter, D. D. Nelson, M. S. Zahniser, D. E. Glenn, R. M. McGovern, *Appl. Phys. B* **2008**, *92*, 387.
[5] E. C. Richard, K. K. Kelly, R. H. Winkler, R. Wilson, T. L. Thompson, R. J. McLaughlin, A. L. Schmeltekopf, A. F. Tuck, *Appl. Phys. B* **2002**, *75*, 183.
[6] W. Chen, R. Maamary, X. Cui, T. Wu, E. Fertein, D. Dewaele, F. Cazier, Q. Zha, Z. Xu, T. Wang, Y. Wang, W. Zang, L. Gao, W. Liu, F. Dong, *Wonder of Nanotechnology Quantum Optoelectronic Devices and Applications* (Eds: M. Razeghi, L. Esaki, K. von Klitzing), SPIE Press, Bellingham, WA **2013**, pp. 693–737.
[7] T. A. Aarhaug, A. Ferber, H. Gaertner, S. Kolås, S. O. Ryman, P. Geiser, *Light Metals* (Ed: O. Martin), Springer International Publishing, Cham **2018**, p. 1487.

[8] P. R. Griffiths, J. A. De Haseth, *Fourier Transform Infrared Spectrometry*, John Wiley & Sons, New York **2007**.
[9] P. L. Hanst, A. S. Lefohn, B. W. Gay, jr., *Appl. Spectrosc.* **1973**, *27*, 188.
[10] M. Erfan, Y. M. Sabry, M. Sakr, B. Mortada, M. Medhat, D. Khalil, *Appl. Spectrosc.* **2016**, *70*, 897.
[11] N. A. Saliba, H. Yang, B. J. Finlayson-Pitts, *J. Phys. Chem. A* **2001**, *105*, 10339.
[12] F. A. F. Winiberg, T. J. Dillon, S. C. Orr, C. B. M. Groß, I. Bejan, C. A. Brumby, M. J. Evans, S. C. Smith, D. E. Heard, P. W. Seakins, *Atmos. Chem. Phys.* **2016**, *16*, 4023.
[13] B. T. Thompson, B. Mizaikoff, *Appl. Spectrosc.* **2006**, *60*, 272.
[14] J. Heland, K. Schäfer, *Atmos. Environ.* **1998**, *32*, 3067.
[15] M. Adachi, Y. Yamagishi, K. Inoue, K. Ishida, *Automotive Emission Analyses Using FTIR Spectrophotometer* **1992**.
[16] D. W. T. Griffith, *Handbook of Vibrationl Spectroscopy*, John Wiley & Sons, New York **2006**.
[17] F. M. Kelliher, A. R. Reisinger, R. J. Martin, M. J. Harvey, S. J. Price, R. R. Sherlock, *Agric. For. Meteorol.* **2002**, *111*, 29.
[18] J. W. Childers, E. L. Thompson Jr, D. B. Harris, D. A. Kirchgessner, M. Clayton, D. F. Natschke, W. J. Phillips, *Atmos. Environ.* **2001**, *35*, 1923.
[19] M. Grutter, E. Flores, R. Basaldud, L. G. Ruiz-Suárez, *Atmos. Oceanic Opt.* **2003**, *16*, 232.
[20] L. A. Todd, M. Ramanathan, K. Mottus, R. Katz, A. Dodson, G. Mihlan, *Atmos. Environ.* **2001**, *35*, 1937.
[21] C. Oppenheimer, P. Francis, M. Burton, A. J. H. Maciejewski, L. Boardman, *Appl. Phys. B* **1998**, *67*, 505.
[22] R. J. Yokelson, I. T. Bertschi, T. J. Christian, P. V. Hobbs, D. E. Ward, W. M. Hao, *J. Geophys. Res.: Atmos.* **2003**, *108*.
[23] A. Miklós, P. Hess, Z. Bozóki, *Rev. Sci. Instrum.* **2001**, *72*, 1937.
[24] A. Miklós, S.-C. Pei, A. H. Kung, *Appl. Opt.* **2006**, *45*, 2529.
[25] A. Keller, M. Rüegg, M. Forster, M. Loepfe, R. Pleisch, P. Nebiker, H. Burtscher, *Sens. Actuators, B* **2005**, *104*, 1.
[26] J. Wojtas, F. K. Tittel, T. Stacewicz, Z. Bielecki, R. Lewicki, J. Mikolajczyk, M. Nowakowski, D. Szabra, P. Stefanski, J. Tarka, *Int. J. Thermophys.* **2014**, *35*, 2215.
[27] J. Huber, C. Weber, A. Eberhardt, J. Wöllenstein, *Procedia Eng* **2016**, *168*, 3.
[28] J. Karhu, T. Tomberg, F. S. Vieira, G. Genoud, V. Hänninen, M. Vainio, M. Metsälä, T. Hieta, S. Bell, L. Halonen, *Opt. Lett.* **2019**, *44*, 1142.
[29] J. Zhou, G. Meng, Y. Zheng, Y. Peng, J. Zou, 45th Int. Conf. on Environmental Systems, **2015**.
[30] F. J. M. Harren, J. Mandon, S. M. Cristescu, *Encycl. Anal. Chem. Appl. Theory Instrum.* **2006**, *3*, 2203.
[31] J. Jiang, Z. Wang, X. Han, C. Zhang, G. Ma, C. Li, Y. Luo, *IEEE Trans. Dielectr. Electr. Insul.* **2019**, *26*, 153.
[32] J. Hodgkinson, R. P. Tatam, *Meas. Sci. Technol.* **2012**, *24*, 012004.
[33] T. Tomberg, M. Vainio, T. Hieta, L. Halonen, *Sci. Rep.* **2018**, *8*, 1848.
[34] Z. Du, S. Zhang, J. Li, N. Gao, K. Tong, *Appl. Sci.* **2019**, *9*, 338.
[35] M. A. Bolshov, Y. A. Kuritsyn, Y. V. Romanovskii, *Spectrochim. Acta, Part B* **2015**, *106*, 45.
[36] Y. Yao, A. J. Hoffman, C. F. Gmachl, *Nat. Photonics* **2012**, *6*, 432.
[37] F. K. Tittel, R. Lewicki, R. Lascola, S. McWhorter, *Trace Analysis of Speciality and Electronics Gases*, Wiley, Hoboken, NJ **2013**, p. 71.
[38] K. E. Whittaker, *Development and Application of Spectroscopic Techniques in the Mid-Infrared*, Oxford University Press, Oxford, UK **2014**.
[39] M. W. Raynor, K. A. Bertness, K. C. Cossel, F. Adler, J. Ye, *Trace Analysis of Speciality and Electronic Gases* (Eds: W. M. Geiger, M. W. Raynor), John Wiley & Sons, New York **2013**, p. 195.
[40] S. Bergin, *Pathlength Calibration of Integrating Sphere Based Gas Cells*, Cranfield University, **2016**.
[41] J. Hodgkinson, D. Masiyano, R. P. Tatam, *Appl. Phys. B* **2010**, *100*, 291.
[42] S. Schilt, F. K. Tittel, K. P. Petrov, *Encycl. Anal. Chem. Appl. Theory Instrum.* **2011**, 1.
[43] M. Pushkarsky, M. Weida, T. Day, D. Arnone, R. Pritchett, D. Caffey, *Rev. Laser Eng.* **2008**, *36*, 80.
[44] A. Rogalski, *Infrared Detectors*, CRC Press, Boca Raton, FL **2010**.
[45] A. Rogalski, M. Kopytko, P. Martyniuk, *Antimonide-Based Infrared Detect: A New Perspective*, SPIE **2018**.
[46] M. Dong, C. Zheng, D. Yao, G. Zhong, S. Miao, W. Ye, Y. Wang, F. K. Tittel, *Opt. Express* **2018**, *26*, 12081.
[47] C. Li, L. Shao, H. Meng, J. Wei, X. Qiu, Q. He, W. Ma, L. Deng, Y. Chen, *Opt. Express* **2018**, *26*, 29330.
[48] H. Gao, L. Xie, P. Gong, H. Wang, *Photonic Sens.* **2018**, *8*, 303.
[49] A. V. Shcherbakova, D. R. Anfimov, I. L. Fufurin, I. S. Golyak, I. A. Trapeznikova, E. R. Kareva, A. N. Morozov, *Opt. Spectrosc.* **2021**, *129*, 1.
[50] K. Krzempek, M. Jahjah, P. Lewicki Rafałand Stefański, S. So, D. Thomazy, F. K. Tittel, *Appl. Phys. B* **2013**, *112*, 461.
[51] C. Li, L. Dong, C. Zheng, F. K. Tittel, *Sens. Actuators, B* **2016**, *232*, 188.
[52] C. Li, C. Zheng, L. Dong, W. Ye, F. K. Tittel, Y. Wang, *Appl. Phys. B* **2016**, *122*, 185.
[53] Q. Gao, Y. Zhang, J. Yu, S. Wu, Z. Zhang, F. Zheng, X. Lou, W. Guo, *Sens. Actuators, A* **2013**, *199*, 106.
[54] W. Ren, W. Jiang, F. K. Tittel, *Appl. Phys. B* **2014**, *117*, 245.
[55] F. Song, C. Zheng, D. Yu, Y. Zhou, W. Yan, W. Ye, Y. Zhang, Y. Wang, F. K. Tittel, *Appl. Phys. B* **2018**, *124*, 51.
[56] X. Cui, F. Dong, Z. Zhang, P. Sun, H. Xia, E. Fertein, W. Chen, *Atmos. Environ.* **2018**, *189*, 125.
[57] B. Li, C. Zheng, H. Liu, Q. He, W. Ye, Y. Zhang, J. Pan, Y. Wang, *Sens. Actuators, B* **2016**, *225*, 188.
[58] Y. Cao, N. P. Sanchez, W. Jiang, R. J. Griffin, F. Xie, L. C. Hughes, C. Zah, F. K. Tittel, *Opt. Express* **2015**, *23*, 2121.
[59] N. M. Davis, J. Hodgkinson, D. Francis, R. P. Tatam, Conf. on Optical Sensing and Detection IV 2016.
[60] D. Francis, J. Hodgkinson, B. Livingstone, P. Black, R. P. Tatam, *Appl. Opt.* **2016**, *55*, 6797.
[61] W. Liang, Y. Bi, Q. Zhou, X. Dong, T. Lv, *Sens. Actuators, B* **2018**, *255*, 2614.
[62] L. Liu, B. Xiong, Y. Yan, J. Li, Z. Du, *IEEE Photonics Technol. Lett.* **2016**, *28*, 1613.
[63] C.-T. Zheng, W.-L. Ye, J.-Q. Huang, T.-S. Cao, M. Lv, J.-M. Dang, Y.-D. Wang, *Sens. Actuators, B* **2014**, *190*, 249.
[64] M. Nikodem, G. Plant, D. Sonnenfroh, G. Wysocki, *Appl. Phys. B* **2015**, *119*, 3.
[65] N. Liu, L. Xu, S. Zhou, L. Zhang, J. Li, *ACS Sens.* **2020**, *5*, 3607.
[66] J. Xia, C. Feng, F. Zhu, S. Zhang, A. A. Kolomenskii, J. Dong, H. A. Schuessler, *Measurement* **2021**, *168*, 108467.
[67] J. Xia, C. Feng, F. Zhu, S. Ye, S. Zhang, A. Kolomenskii, Q. Wang, J. Dong, Z. Wang, W. Jin, H. A. Schuessler, *Sens. Actuators, B* **2021**, *334*, 129641.
[68] S. Viciani, F. D'amato, P. Mazzinghi, F. Castagnoli, G. Toci, P. Werle, *Appl. Phys. B* **2008**, *90*, 581.
[69] R. Cui, L. Dong, H. Wu, S. Li, L. Zhang, W. Ma, W. Yin, L. Xiao, S. Jia, F. K. Tittel, *Opt. Express* **2018**, *26*, 24318.
[70] K. Shibuya, A. Podzorov, M. Matsuhama, K. Nishimura, M. Magari, *Meas. Sci. Technol.* **2020**, *32*, 035201.
[71] X. Li, F. Yuan, M. Hu, B. Chen, Y. He, C. Yang, L. Shi, R. Kan, *Sensors* **2020**, *20*, 1910.
[72] T. Wu, W. Kong, M. Wang, Q. Wu, W. Chen, C. Ye, R. Hu, X. He, *J. Lightwave Technol.* **2020**, *38*, 4580.
[73] W. Ren, L. Luo, F. K. Tittel, *Sens. Actuators, B* **2015**, *221*, 1062.
[74] L. Dong, Y. Yu, C. Li, S. So, F. K. Tittel, *Opt. Express* **2015**, *23*, 19821.
[75] W. Ren, L. Luo, Y. Cao, W. Jiang, F. K. Tittel, *Conf. on Quantum Sens. Nanophotonic Devices*, XII 2015, p. 93702B.

[76] L. Long, W. Xie, X. Yang, *Optik* **2016**, *127*, 8277.
[77] I. M. Craig, B. D. Cannon, M. S. Taubman, B. E. Bernacki, R. D. Stahl, J. T. Schiffern, T. L. Myers, M. C. Phillips, *Appl. Phys. B* **2015**, *120*, 505.
[78] C. L. Schiller, S. Locquiao, T. J. Johnson, G. W. Harris, *J. Atmos. Chem.* **2001**, *40*, 275.
[79] F. Stritzke, O. Diemel, S. Wagner, *Appl. Phys. B* **2015**, *119*, 143.
[80] D. I. Herman, C. Weerasekara, L. C. Hutcherson, F. R. Giorgetta, K. C. Cossel, E. M. Waxman, G. M. Colacion, N. R. Newbury, S. M. Welch, B. D. DePaola, I. Coddington, E. A. Santos, B. R. Washburn, *Sci. Adv.* **2021**, *7*, 9765.
[81] D. J. Miller, K. Sun, L. Tao, M. A. Khan, M. A. Zondlo, *Atmos. Meas. Tech.* **2014**, *7*, 81.
[82] G. J. Fetzer, A. S. Pittner, W. L. Ryder, D. A. Brown, *Appl. Opt.* **2002**, *41*, 3613.
[83] R. Claps, F. V. Englich, D. P. Leleux, D. Richter, F. K. Tittel, R. F. Curl, *Appl. Opt.* **2001**, *40*, 4387.
[84] A. R. Kost, *MRS Online Proc. Libr.* **1997**, *484*, 3.
[85] A. Bauer, K. Rößner, T. Lehnhardt, M. Kamp, S. Höfling, L. Worschech, A. Forchel, *Semicond. Sci. Technol.* **2010**, *26*, 014032.
[86] J. Hecht, *The Laser Guidebook*, McGraw-Hill, New York, NY **1986**.
[87] M. Tacke, *Philos. Trans. R. Soc. London, Ser. A* **2001**, *359*, 547.
[88] J. Faist, F. Capasso, D. L. Sivco, C. Sirtori, A. L. Hutchinson, A. Y. Cho, *Science* **1994**, *264*, 553.
[89] N. Bandyopadhyay, M. Chen, S. Sengupta, S. Slivken, M. Razeghi, *Opt. Express* **2015**, *23*, 21159.
[90] I. Vurgaftman, R. Weih, M. Kamp, J. R. Meyer, C. L. Canedy, C. S. Kim, M. Kim, W. W. Bewley, C. D. Merritt, J. Abell, S. Höfling, *J. Phys. D. Appl. Phys.* **2015**, *48*, 123001.
[91] W. Nakwaski, S. Grzempa, M. Dems, T. Czyszanowski, 20th *Int. Conf. on Transparent Optical Networks* **2018**, *1*.
[92] W. W. Bewley, C. L. Canedy, C. S. Kim, C. D. Merritt, M. V. Warren, I. Vurgaftman, J. R. Meyer, M. Kim, *Appl. Phys. Lett.* **2016**, *109*, 151108.
[93] D. Richter, A. Fried, P. Weibring, *Laser Photonics Rev.* **2009**, *3*, 343.
[94] Y. Chen, M. Soskind, J. McSpiritt, R. Wang, N. Li, M. Zondlo, G. Wysocki, *2019 Conf. on Lasers Electro-Optics* **2019**, p. 1.
[95] J. U. White, *JOSA* **1942**, *32*, 285.
[96] D. R. Herriott, H. J. Schulte, *Appl. Opt.* **1965**, *4*, 883.
[97] J. B. McManus, P. L. Kebabian, M. S. Zahniser, *Appl. Opt.* **1995**, *34*, 3336.
[98] M. L. Thoma, R. Kaschow, F. J. Hindelang, *Shock Waves* **1994**, *4*, 51.
[99] M. W. Sigrist, R. Bartlome, D. Marinov, J. M. Rey, D. E. Vogler, H. Wächter, *Appl. Phys. B* **2008**, *90*, 289.
[100] R. Stach, J. Haas, E. Tütüncü, S. Daboss, C. Kranz, B. Mizaikoff, *ACS Sens.* **2017**, *2*, 1700.
[101] E. Hawe, C. Fitzpatrick, P. Chambers, G. Dooly, E. Lewis, *Sens. Actuators, A* **2008**, *141*, 414.
[102] B. T. Thompson, A. Inberg, N. Croitoru, B. Mizaikoff, *Appl. Spectrosc.* **2006**, *60*, 266.
[103] Y. Matsuura, M. Miyagi, *Appl. Opt.* **1993**, *32*, 6598.
[104] J. M. Kriesel, N. Gat, B. E. Bernacki, R. L. Erikson, B. D. Cannon, T. L. Myers, C. M. Bledt, J. A. Harrington, *Conf. Chemical, Biological, Radiological, Nuclear, and Explosives (CBRNE)* Sensing XII **2011**.
[105] A. Wilk, J. C. Carter, M. Chrisp, A. M. Manuel, P. Mirkarimi, J. B. Alameda, B. Mizaikoff, *Anal. Chem.* **2013**, *85*, 11205.
[106] D. Romanini, I. Ventrillard, G. Méjean, J. Morville, E. Kerstel, in *Cavity-Enhanced Spectroscopy And Sensing*, Springer, Berlin **2014**, p. 1.
[107] S. S. Brown, *Chem. Rev.* **2003**, *103*, 5219.
[108] A. Foltynowicz, F. M. Schmidt, W. Ma, O. Axner, *Appl. Phys. B* **2008**, *92*, 313.
[109] G. Berden, R. Engeln, *Cavity Ring-down Spectroscopy: Techniques and Applications*, John Wiley & Sons, New York **2009**.
[110] F. Wang, J. Chang, Q. Wang, W. Wei, Z. Qin, *Sens. Actuators, A* **2017**, *259*, 152.
[111] A. Rogalski, *Prog. Quantum Electron.* **2003**, *27*, 59.
[112] H. Photonics, *Characteristics and use of infrared detectors*, Hamamatsu city, Japan **2004**.
[113] A. Rogalski, *Opto-Electron. Rev.* **2012**, *20*, 279.
[114] https://vigo.com.pl/ (accessed: April 2022) Optical detectors supplier.
[115] https://www.hamamatsu.com (accessed: April 2022) Optical detector supplier.
[116] C. Dyroff, *Tunable Diode Laser Absorption Spectroscopy for Trace Gas Measurements with High Sensitivity and Low Drift*, University-Verlag, **2009**.
[117] R. Yang, X. Dong, Y. Bi, T. Lv, *Opt. Commun.* **2018**, *410*, 782.
[118] J. M. Nicely, T. F. Hanisco, H. Riris, *J. Quant. Spectrosc. Radiat. Transfer* **2018**, *211*, 115.
[119] A. Klein, O. Witzel, V. Ebert, *Sensors* **2014**, *14*, 21497.
[120] X. Chao, J. B. Jeffries, R. K. Hanson, *Appl. Phys. B* **2012**, *106*, 987.
[121] I. D. Lindsay, P. Groß, C. J. Lee, B. Adhimoolam, K.-J. Boller, *Opt. Express* **2006**, *14*, 12341.
[122] F. S. Pavone, M. Inguscio, *Appl. Phys. B* **1993**, *56*, 118.
[123] M. Niu, Q. Liu, K. Liu, Y. Yuan, X. Gao, *Opt. Commun.* **2013**, *287*, 180.
[124] M. Vainio, L. Halonen, *Phys. Chem. Chem. Phys.* **2016**, *18*, 4266.
[125] J. Kauppinen, K. Wilcken, I. Kauppinen, V. Koskinen, *Microchem. J.* **2004**, *76*, 151.
[126] T. Kuusela, J. Kauppinen, *Appl. Spectrosc. Rev.* **2007**, *42*, 443.
[127] E. W. Slocum, *AIChE J.* **1956**, *2*, 11D.
[128] T. Laurila, H. Cattaneo, T. Pöyhönen, V. Koskinen, J. Kauppinen, R. Hernberg, *Appl. Phys. B* **2006**, *83*, 285.
[129] A. Glière, J. Rouxel, M. Brun, B. Parvitte, V. Zéninari, S. Nicoletti, *Sensors* **2014**, *14*, 957.
[130] P. D. Edmonds, J. Lamb, *Proc. Phys. Soc.* **1958**, *72*, 940.
[131] D. Weaner, J. F. Roach, W. R. Smith, *J. Chem. Phys.* **1967**, *47*, 3096.
[132] J. C. F. Wang, G. S. Springer, *J. Chem. Phys.* **1973**, *59*, 6556.
[133] J. L. Stretton, *Trans. Faraday Soc.* **1965**, *61*, 1053.
[134] A. Elia, P. M. Lugarà, C. Di Franco, V. Spagnolo, *Sensors* **2009**, *9*, 9616.
[135] S. Schilt, J.-P. Besson, L. Thévenaz, *J. Phys. IV* **2005**, *125*, 7.
[136] D. P. E. Smith, *Rev. Sci. Instrum.* **1995**, *66*, 3191.
[137] F. R. Blom, S. Bouwstra, M. Elwenspoek, J. H. J. Fluitman, *J. Vac. Sci. Technol., B: Microelectron. Nanometer Struct. – Process., Meas., Phenom.* **1992**, *10*, 19.
[138] D. R. Lide, *CRC Handbook of Chemistry and Physics: A Ready-Reference Book of Chemical and Physical Data*, CRC Press, Boca Raton, FL **1995**.
[139] K. Chen, X. Zhou, Z. Gong, S. Yu, C. Qu, M. Guo, Q. Yu, *2017 Int. Conf. Optical on Instruments and Technolology: Optoelectronic Measurement Technology and System* **2018**, p. 1062108.
[140] K. Chen, B. Zhang, S. Liu, Q. Yu, *Sens. Actuators, B* **2019**, *283*, 1.
[141] W. Wei, Y. Zhu, C. Lin, L. Tian, Z. Xu, J. Nong, *Int. J. Thermophys.* **2015**, *36*, 1116.
[142] J. Suchánek, M. Dostál, T. Vlasáková, P. Janda, M. Klusáčková, P. Kubát, V. Nevrlý, P. Bitala, S. Civiš, Z. Zelinger, *Measurement* **2017**, *101*, 9.
[143] P. G. Westergaard, M. Lassen, *Appl. Opt.* **2016**, *55*, 8266.
[144] T. Kuusela, J. Peura, B. A. Matveev, M. A. Remennyy, *Vib. Spectrosc.* **2009**, *51*, 289.
[145] R. Coutu, I. Medvedev, D. Petkie, *Sensors* **2016**, *16*, 251.
[146] N. E. Glauvitz, R. A. Coutu, I. R. Medvedev, D. T. Petkie, *J. Microelectromech. Syst.* **2015**, *24*, 216.
[147] J. Fonsen, V. Koskinen, K. Roth, J. Kauppinen, *Vib. Spectrosc.* **2009**, *50*, 214.
[148] N. Ledermann, P. Muralt, J. Baborowski, M. Forster, J.-P. Pellaux, *J. Micromech. Microeng.* **2004**, *14*, 1650.

[149] S. Zhou, M. Slaman, D. Iannuzzi, *Opt. Express* **2017**, *25*, 17541.
[150] J. Saarela, J. Toivonen, A. Manninen, T. Sorvajärvi, R. Hernberg, *Appl. Opt.* **2009**, *48*, 743.
[151] K. Chen, Z. Yu, Z. Gong, Q. Yu, *Opt. Lett.* **2018**, *43*, 5038.
[152] B. D. Adamson, J. E. Sader, E. J. Bieske, *J. Appl. Phys.* **2009**, *106*, 114510.
[153] E. D. McNaghten, K. A. Grant, A. M. Parkes, P. A. Martin, *Appl. Phys. B* **2012**, *107*, 861.
[154] A. Szabó, A. Mohacsi, G. Gulyas, Z. Bozoki, G. Szabo, *Meas. Sci. Technol.* **2013**, *24*, 065501.
[155] E. L. Holthoff, D. A. Heaps, P. M. Pellegrino, *IEEE Sens. J.* **2010**, *10*, 572.
[156] A. A. Kosterev, Y. A. Bakhirkin, R. F. Curl, F. K. Tittel, *Opt. Lett.* **2002**, *27*, 1902.
[157] Q. Wang, J. Wang, L. Li, Q. Yu, *Sens. Actuators, B* **2011**, *153*, 214.
[158] Y. Cao, W. Jin, H. L. Ho, J. Ma, *Opt. Lett.* **2013**, *38*, 434.
[159] A. Kachanov, S. Koulikov, F. K. Tittel, *Appl. Phys. B* **2013**, *110*, 47.
[160] R. E. Lindley, A. M. Parkes, K. A. Keen, E. D. McNaghten, A. J. Orr-Ewing, *Appl. Phys. B* **2007**, *86*, 707.
[161] K. Wilcken, J. Kauppinen, *Appl. Spectrosc.* **2003**, *57*, 1087.
[162] C. B. Hirschmann, J. Lehtinen, J. Uotila, S. Ojala, R. L. Keiski, *Appl. Phys. B* **2013**, *111*, 603.
[163] V. Zeninari, B. Parvitte, D. Courtois, V. A. Kapitanov, Y. N. Ponomarev, *Infrared Phys. Technol.* **2003**, *44*, 253.
[164] L. Liu, H. Huan, A. Mandelis, L. Zhang, C. Guo, W. Li, X. Zhang, X. Yin, X. Shao, D. Wang, *Opt. Laser Technol.* **2022**, *148*, 107695.
[165] V. Spagnolo, P. Patimisco, R. Pennetta, A. Sampaolo, G. Scamarcio, M. S. Vitiello, F. K. Tittel, *Opt. Express* **2015**, *23*, 7574.
[166] P. Patimisco, S. Borri, I. Galli, D. Mazzotti, G. Giusfredi, N. Akikusa, M. Yamanishi, G. Scamarcio, P. De Natale, V. Spagnolo, *Analyst* **2015**, *140*, 736.
[167] Y. He, Y. Ma, Y. A. O. Tong, X. I. N. Yu, F. K. Tittel, *Opt. Lett.* **2019**, *44*, 1904.
[168] A. A. Kosterev, P. R. Buerki, L. Dong, M. Reed, T. Day, F. K. Tittel, *Appl. Phys. B* **2010**, *100*, 173.
[169] V. Spagnolo, P. Patimisco, S. Borri, G. Scamarcio, B. E. Bernacki, J. Kriesel, *Appl. Phys. B* **2013**, *112*, 25.
[170] A. Sampaolo, P. Patimisco, M. Giglio, M. Vitiello, H. Beere, D. Ritchie, G. Scamarcio, F. K. Tittel, V. Spagnolo, *Sensors* **2016**, *16*, 439.
[171] I. Sadiek, T. Mikkonen, M. Vainio, J. Toivonen, A. Foltynowicz, *Phys. Chem. Chem. Phys.* **2018**, *20*, 27849.
[172] V. Spagnolo, P. Patimisco, A. Sampaolo, M. Giglio, F. K. Tittel, *Opt. Photonics Energy Environ.* **2017**, ETh1A–6.
[173] J. Rakovský, O. Votava, *Rev. Sci. Instrum.* **2017**, *88*, 013103.
[174] K. Chen, Z. Gong, M. Guo, S. Yu, C. Qu, X. Zhou, Q. Yu, *Sens. Actuators, A* **2018**, *279*, 107.
[175] K. Liu, Y. Cao, G. Wang, W. Zhang, W. Chen, X. Gao, *Sens. Actuators, B* **2018**, *277*, 571.
[176] N. E. Glauvitz, R. A. Coutu, M. Kistler, I. R. Medvedev, D. T. Petkie, *MEMS Nanotechnology*, Vol. 5, Springer, Berlin **2014**, p. 73.
[177] S. Zhou, D. Iannuzzi, *Rev. Sci. Instrum.* **2019**, *90*, 023102.
[178] J. Uotila, V. Koskinen, J. Kauppinen, *Vib. Spectrosc.* **2005**, *38*, 3.
[179] I. Kauppinen **2009**, *US Patent* 7,521,668.
[180] Z. Yu, A. Wang, *IEEE Photonics Technol. Lett.* **2015**, *27*, 817.
[181] G. Gruca, K. Heeck, J. Rector, D. Iannuzzi, *Opt. Lett.* **2013**, *38*, 1672.
[182] Y. Cao, W. Jin, H. L. Ho, L. Qi, Y. H. Yang, *Appl. Phys. B* **2012**, *109*, 359.
[183] H. Moser, B. Lendl, *Appl. Phys. B* **2016**, *122*, 83.
[184] T. Tomberg, T. Hieta, M. Vainio, L. Halonen, *Analyst* **2019**, *144*, 2291.
[185] V. Koskinen, J. Fonsen, J. Kauppinen, I. Kauppinen, *Vib. Spectrosc.* **2006**, *42*, 239.
[186] K. Keränen, J. Ollila, H. Saloniemi, B. Matveev, J. Raittila, A. Helle, I. Kauppinen, T. Kuusela, L. Pierno, P. Karioja, M. Karppinen, *Procedia Eng.* **2012**, *47*, 1438.
[187] Z. Zelinger, P. Janda, J. Suchánek, M. Dostál, P. Kubát, V. Nevrly, P. Bitala, S. Civiš, *J. Sensors Sens. Syst.* **2015**, *4*, 103.
[188] J. Suchánek, P. Janda, M. Dostál, A. Knížek, P. Kubát, P. Roupcová, P. Bitala, V. Nevrly, Z. Zelinger, *Microchem. J.* **2019**, *144*, 203.
[189] W. Li, Z. Wang, C. Feng, Q. Li, H. Yu, *Sens. Actuators, A* **2019**, *285*, 300.
[190] N. Glauvitz, S. Blazevic, R. Coutu Jr, M. Kistler, I. R. Medvedev, D. Petkie, *Procedia Eng.* **2012**, *47*, 730.
[191] J. Czarny, A. Walther, B. Desloges, P. Robert, E. Redon, T. Verdot, K. Ege, C. Guianvarc'h, J.-L. Guyader, *2013 Int. Semicondoctor Conf. Dresden-Grenoble* **2013**, p. 1.
[192] T. Hu, B. Dong, X. Luo, T.-Y. Liow, J. Song, C. Lee, G.-Q. Lo, *Photonics Res.* **2017**, *5*, 417.
[193] S. Nicoletti, P. Barritault, S. Boutami, M. Brun, A. Gliere, P. Labeye, J. Rouxel, J. Czarny, H. Lhermet, M. Carras, G. Maisons, *Conf. IEEE Sensors*.
[194] K. Chen, H. Deng, M. Guo, C. Luo, S. Liu, B. Zhang, F. Ma, F. Zhu, Z. Gong, W. Peng, Q. Yua, *Opt. Laser Technol.* **2020**, *123*, 105894.
[195] M. Guo, K. Chen, C. Li, L. Xu, G. Zhang, N. Wang, C. Li, F. Ma, Z. Gong, Q. Yu, *Anal. Chem.* **2022**, *94*, 1151.
[196] F. Ma, Z. Liao, Y. Zhao, Z. Qiu, L. Wan, K. Li, G. Zhang, *Optik* **2021**, *232*, 166525.
[197] H. Cheng, J. Tang, X. Zhang, Y. Li, J. Hu, Y. Zhang, S. Mao, S. Xiao, *IEEE Trans. Instrum. Meas.* **2021**, *70*, 1.
[198] H. Cheng, X. Zhang, C. Bian, J. Cheng, Z. Chen, Y. Zhang, J. Tang, S. Xiao, *AIP Adv.* **2020**, *10*, 105122.
[199] M. Fatima, T. Hausmaninger, T. Tomberg, J. Karhu, M. Vainio, T. Hieta, G. Genoud, *Opt. Lett.* **2021**, *46*, 2083.
[200] A. M. Parkes, K. A. Keen, E. D. McNaghten, *Conf. Fiber Opt. Sensors Appl.* V, 2007, 67701C.
[201] F. Xin, D. Yang, C. Li, W. Yan, Y. Wang, *Int. Conf. on Optoelectronics and Microelectronics Technology and Application* **2020**, p. 1161722.
[202] A. Gliere, P. Barritault, A. Berthelot, C. Constancias, J.-G. Coutard, B. Desloges, L. Duraffourg, J.-M. Fedeli, M. Garcia, O. Lartigue, H. Lhermet, A. Marchant, J. Rouxel, J. Skubich, A. Teulle, T. Verdot, S. Nicoletti, *Int. J. Thermophys.* **2020**, *41*, 1.
[203] J. Karhu, H. Philip, A. Baranov, R. Teissier, T. Hieta, *Opt. Lett.* **2020**, *45*, 5962.
[204] S. Larnimaa, J. Karhu, T. Tomberg, G. Genoud, T. Hieta, M. Metsälä, L. Halonen, M. Vainio, *2020 Conf. on Lasers Electro-Optics* **2020**, p. 1.
[205] C. Li, M. Guo, B. Zhang, C. Li, B. Yang, K. Chen, *Opt. Lasers Eng.* **2022**, *149*, 106792.
[206] Y. Jiao, H. Fan, Z. Gong, K. Yang, F. Shen, K. Chen, L. Mei, W. Peng, Q. Yu, *Appl. Sci.* **2021**, *11*, 4997.
[207] Z. Gong, T. Gao, L. Mei, K. Chen, Y. Chen, B. Zhang, W. Peng, Q. Yu, *Photoacoustics* **2021**, *21*, 100216.
[208] H. Cattaneo, T. Laurila, R. Hernberg, *Appl. Phys. B* **2006**, *85*, 337.
[209] H. Panu, R. Timo, F. Thomas, J. Makkonen, S. Alyshev, A. Kharakhordin, S. Firstov, *Meas. Sci. Technol.* **2021**, *32*, 055206.
[210] J. Peltola, T. Hieta, M. Vainio, *Opt. Lett.* **2015**, *40*, 2933.
[211] Z. Gong, T. Gao, Y. Chen, B. Zhang, W. Peng, Q. Yu, F. Ma, L. Mei, K. Chen, *J. Quant. Spectrosc. Radiat. Transfer* **2020**, *253*, 107136.
[212] J. Karhu, T. Hieta, F. Manoocheri, M. Vainio, E. Ikonen, *ACS Sens.* **2021**, *6*, 3303.
[213] J. Karhu, T. Hieta, *Appl. Opt.* **2022**, *61*, 1892.
[214] S. Campbell, *Development of Idealized Practices for Photoacoustic Spectroscopy*, Memorial University of Newfoundland, Canada **2017**.
[215] A. M. Othman, H. E. Kotb, Y. M. Sabry, D. Khalil, *Appl. Spectrosc.* **2020**, *74*, 799.
[216] W. Denzer, M. L. Hamilton, G. Hancock, M. Islam, C. E. Langley, R. Peverall, G. A. D. Ritchie, *Analyst* **2009**, *134*, 2220.
[217] D. J. Lahneman, T. J. Huffman, P. Xu, S. L. Wang, T. Grogan, M. M. Qazilbash, *Opt. Express* **2017**, *25*, 20421.
[218] D. K. Smith **2008**, *US Patent* 7,435,982.

[219] H. Zhu, P. Blackborow, *Laser Focus World* **2011**, *47*, 53.
[220] A. Khodabakhsh, V. Ramaiah-Badarla, L. Rutkowski, A. C. Johansson, K. F. Lee, J. Jiang, C. Mohr, M. E. Fermann, A. Foltynowicz, *Opt. Lett.* **2016**, *41*, 2541.
[221] N. Picqué, T. W. Hänsch, *Nat. Photonics* **2019**, *13*, 146.
[222] K. C. Cossel, E. M. Waxman, I. A. Finneran, G. A. Blake, J. Ye, N. R. Newbury, *J. Opt. Soc. Am. B* **2017**, *34*, 104.
[223] I. Coddington, N. Newbury, W. Swann, *Optica* **2016**, *3*, 414.
[224] K. C. Cossel, E. M. Waxman, F. R. Giorgetta, M. Cermak, I. R. Coddington, D. Hesselius, S. Ruben, W. C. Swann, G.-W. Truong, G. B. Rieker, N. R. Newbury, *Optica* **2017**, *4*, 724.
[225] G. Ycas, F. R. Giorgetta, K. C. Cossel, E. M. Waxman, E. Baumann, N. R. Newbury, I. Coddington, *Optica* **2019**, *6*, 165.
[226] S.-S. Kim, N. Menegazzo, C. Young, J. Chan, C. Carter, B. Mizaikoff, *Appl. Spectrosc.* **2009**, *63*, 331.
[227] A. A. Ruth, J. Orphal, S. E. Fiedler, *Appl. Opt.* **2007**, *46*, 3611.
[228] J. Orphal, A. A. Ruth, *Opt. Express* **2008**, *16*, 19232.
[229] D. M. O'Leary, A. A. Ruth, S. Dixneuf, J. Orphal, R. Varma, *J. Quant. Spectrosc. Radiat. Transfer* **2012**, *113*, 1138.
[230] U. Platt, J. Meinen, D. Pöhler, T. Leisner, *Atmos. Meas. Tech.* **2009**, *2*, 713.
[231] K. Zheng, C. Zheng, Y. Zhang, Y. Wang, F. K. Tittel, *Sensors* **2018**, *18*, 3646.
[232] R. Thalman, M. T. Baeza-Romero, S. M. Ball, E. Borrás, M. J. S. Daniels, I. C. A. Goodall, S. B. Henry, T. Karl, F. N. Keutsch, S. Kim, P. S. Monks, A. Muñoz, J. Orlando, S. Peppe, A. R. Rickard, M. Ródenas, P. Sánchez, R. Seco, L. Su, G. Tyndall, M. Vázquez, T. Vera, E. Waxman, R. Volkamer, *Atmos. Meas. Tech. Discuss.* **2014**, *7*, 8581.
[233] http://hitran.iao.ru/ (accessed: April 2022) "Gases database".
[234] M. B. Esler, D. W. T. Griffith, S. R. Wilson, L. P. Steele, *Anal. Chem.* **2000**, *72*, 206.
[235] P. L. Hanst, N. W. Wong, J. Bragin, *Atmos. Environ.* **1982**, *16*, 969.
[236] S. N. Vardag, S. Hammer, S. O'Doherty, T. G. Spain, B. Wastine, A. Jordan, I. Levin, *Atmos. Chem. Phys.* **2014**, *14*, 8403.
[237] H. H. Funke, M. W. Raynor, B. Yücelen, V. H. Houlding, *J. Electron. Mater.* **2001**, *30*, 1438.
[238] D. Richter, M. Erdelyi, R. F. Curl, F. K. Tittel, C. Oppenheimer, H. J. Duffell, M. Burton, *Opt. Lasers Eng.* **2002**, *37*, 171.
[239] A. Schliesser, N. Picqué, T. W. Hänsch, *Nat. Photonics* **2012**, *6*, 440.
[240] F. Adler, P. Masłowski, A. Foltynowicz, K. C. Cossel, T. C. Briles, I. Hartl, J. Ye, *Opt. Express* **2010**, *18*, 21861.
[241] A. Fathy, Y. M. Sabry, M. Amr, M. Gnambodoe-Capo-chichi, M. Anwar, A. O. Ghoname, A. Amr, A. Saeed, M. Gad, M. Al Haron, M. Erfan, Y. L. Wang, S. Saadany, D. Khalil, T. Bourouina, *MOEMS Miniaturized Systems XVIII* **2019**, p. 1093109.
[242] A. A. Elsayed, M. Sakr, M. Erfan, Y. M. Sabry, D. Khalil, in *2016 33rd National Radio Science Conf.*, **2016**, p. 348.
[243] D. Briand, O. Manzardo, N. F. de Rooij, J. Hildenbrand, J. Wollenstein, *Conf. IEEE Sensors*, 2007, p. 1364.
[244] L. Espinoza-Nava, C. Dubois, E. Batista, *Light Metals*, Springer, Berlin **2020**, pp. 758–765.
[245] J. M. Dorhout, K. Nowak-Lovato, R. K. Carlson, R. P. Currier, A. S. Anderson, E. R. Batista, Z. Li, R. K. Martinez, M. P. Wilkerson, S. M. Clegg, *J. Mol. Spectrosc.* **2020**, *371*, 111307.
[246] A. Fouqueau, M. Cirtog, M. Cazaunau, E. Pangui, J.-F. Doussin, B. Picquet-Varrault, *Atmos. Chem. Phys.* **2020**, *20*, 15167.
[247] T. Hasegawa, *Quantitative Infrared Spectroscopy for Understanding of a Condensed Matter*, Springer, Berlin **2017**.
[248] L. Liu, A. Mandelis, H. Huan, K. Michaelian, A. Melnikov, *Vib. Spectrosc.* **2016**, *87*, 94.
[249] L. Liu, A. Mandelis, A. Melnikov, K. Michaelian, H. Huan, C. Haisch, *Int. J. Thermophys.* **2016**, *37*, 64.
[250] L. Liu, A. Mandelis, H. Huan, *Int. J. Thermophys.* **2018**, *39*, 94.
[251] D. P. Baldwin, R. W. Jones, J. F. McClelland, *Photoacoustic and Photothermal Phenomena III*, Springer, Berlin **1992**, pp. 3–5.
[252] G. Busse, B. Bullemer, *Infrared Phys.* **1978**, *18*, 631.
[253] R. S. Wright, G. B. Howe, R. K. M. Jayanty, *J. Air Waste Manage. Assoc.* **1998**, *48*, 1077.
[254] J. Uotila, J. Kauppinen, *Appl. Spectrosc.* **2008**, *62*, 655.
[255] C. B. Hirschmann, J. Uotila, S. Ojala, J. Tenhunen, R. L. Keiski, *Appl. Spectrosc.* **2010**, *64*, 293.
[256] L. Liu, A. Mandelis, H. Huan, A. Melnikov, *Appl. Phys. B: Lasers Opt.* **2016**, *122*, 1.
[257] T. Mikkonen, C. Amiot, A. Aalto, K. Patokoski, G. Genty, J. Toivonen, *Opt. Lett.* **2018**, *43*, 5094.
[258] S. Larnimaa, L. Halonen, J. Karhu, T. Tomberg, M. Metsälä, G. Genoud, T. Hieta, S. Bell, M. Vainio, *Chem. Phys. Lett.* **2020**, *750*, 137488.
[259] T. Mikkonen, T. Hieta, G. Genty, J. Toivonen, *2021 Conf. on Lasers and Electro-Optics Europe and European Quantum Electronics Conf.*, **2021**, p. 1.
[260] A. G. Griffith, R. K. W. Lau, J. Cardenas, Y. Okawachi, A. Mohanty, R. Fain, Y. H. D. Lee, M. Yu, C. T. Phare, C. B. Poitras, A. L. Gaeta, M. Lipson, *Nat. Commun.* **2015**, *6*, 1.
[261] A. L. Gaeta, M. Lipson, T. J. Kippenberg, *Nat. Photonics* **2019**, *13*, 158.

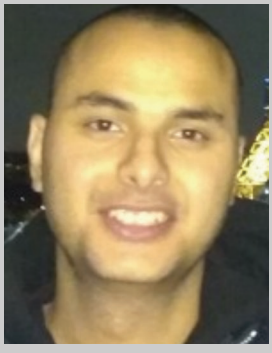

Alaa Fathy received the B.Sc. and M.Sc. degrees in electrical engineering from Ain Shams University, Cairo, Egypt, in 2013 and 2017, respectively. He obtained his Ph.D. from Université Paris-Est, ESIEE Paris, France in 2020. He is currently an assistant professor at Ain Shams University, Faculty of Engineering. His research interests include optical MEMS and gas sensing.

Yasser M. Sabry received the B.Sc. and M.Sc. degrees in electrical engineering from Ain Shams University, Cairo, Egypt, in 2005 and 2009, respectively. He obtained his Ph.D. from Université Paris-Est, ESIEE Paris, France in 2013. He is a holder of the TWAS-ARO Young Arab Scientist prize, Egypt State Encouragement Award in Engineering Science and Mohammed Rabee Nasser Award for Young Scientists in Applied Research. He is currently an associate professor at Ain Shams University and the Head of Optical and Microsystems Technologies Group in Si-Ware Systems Inc. His research interests include spectral sensors, microphotonics, biophotonics, and artificial intelligence.

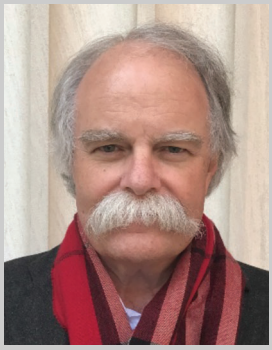

Ian W. Hunter is the Hatsopoulos Professor of Thermodynamics in the Department of Mechanical Engineering at the Massachusetts Institute of Technology (MIT) where he has been a faculty member since 1994. He has over 500 scientific and engineering publications and 120 issued patents. He is a National Academy of Inventors (NAI) Fellow, American Institute for Medical and Biological Engineering Fellow, American Association for the Advancement of Science (AAAS) Fellow, and the recipient of the 2022 IEEE Keithley Award in Instrumentation and Measurement. He has founded or cofounded over 30 companies in a wide variety of disciplines.

Diaa Khalil has over 35 years of experience in micro photonic systems. He obtained his Ph.D. from INPG France in 1993. He is professor of photonics in ASU since 2004. He supervised more than 80 M.Sc. and Ph.D. From 2007 to 2020, he was the CTO of the Optical MEMS Division in Si-Ware Systems. He is inventor of about 25 patents and patent applications, author and coauthor of more than 370 publications, 3 book chapters, and 1 ebook and member in the editorial board of the Light: Science and Applications journal, produced by the Nature PG.

Tarik Bourouina received his Ph.D. in 1991 and his habilitation (HDR) from Université Paris-Saclay. He has been a faculty member since 1992, professor of physics since 2002 at ESIEE Paris, Université Gustave Eiffel and affiliated to the French National Center for Scientific Research (CNRS) within ESYCOM laboratory UMR9007. He was previously at The University of Tokyo, Japan and associate professor at Université Paris-Saclay. Since 2007, he has been Advisory CSO of the MEMS division at Si-ware Systems. He cofounded Fluidion in 2012 and Izonics in 2021. In 2017, he was the recipient of the Chinese Academy of Sciences President's Fellowship.